Cusping, capture, and breakup of interacting drops by a curvatureless boundary-integral algorithm

By ALEXANDER Z. ZINCHENKO,
MICHAEL A. ROTHER AND ROBERT H. DAVIS†

Department of Chemical Engineering, University of Colorado, Boulder, CO 80309-0424, USA

A three-dimensional boundary-integral algorithm for interacting deformable drops in Stokes flow is developed. The algorithm is applicable to very large deformations and extreme cases, including cusped interfaces and drops closely approaching breakup. A new, curvatureless boundary-integral formulation is used, containing only the normal vectors, which are usually much less sensitive than is the curvature to discretization errors. A proper regularization makes the method applicable to small surface separations and arbitrary λ, where λ is the ratio of the viscosities of the drop and medium. The curvatureless form eliminates the difficulty with the concentrated capillary force inherent in two-dimensional cusps and allows simulation of three-dimensional drop/bubble motions with point and line singularities, while the conventional form can only handle point singularities. A combination of the curvatureless form and a special, passive technique for adaptive mesh stabilization allows three-dimensional simulations for high aspect ratio drops closely approaching breakup, using highly stretched triangulations with fixed topology. The code is applied to study relative motion of two bubbles or drops under gravity for moderately high Bond numbers $\mathscr{B}$, when cusping and breakup are typical. The deformation-induced capture efficiency of bubbles and low-viscosity drops is calculated and found to be in reasonable agreement with available experiments of Manga & Stone (1993, 1995*b*). Three-dimensional breakup of the smaller drop due to the interaction with a larger one for $\lambda = O(1)$ is also considered, and the algorithm is shown to accurately simulate both the primary breakup moment and the volume partition by extrapolation for moderately supercritical conditions. Calculations of the breakup efficiency suggest that breakup due to interactions is significant in a sedimenting emulsion with narrow size distribution at $\lambda = O(1)$ and $\mathscr{B} \geqslant 5$–10. A combined capture and breakup phenomenon, when the smaller drop starts breaking without being released from the dimple formed on the larger one, is also observed in the simulations. A general classification of possible modes of two-drop interactions for $\lambda = O(1)$ is made.

1. Introduction

Low Reynolds number motion of deformable drops or bubbles, single or interacting, is a fundamental problem of relevance to emulsion sedimentation/creaming and rheology, and to drop coalescence and breakup. As long as fluid inertia can be neglected, the boundary-integral method (Rallison & Acrivos 1978; Pozrikidis 1992)

† Author to whom correspondence should be addressed: e-mail: robert.davis@colorado.edu.
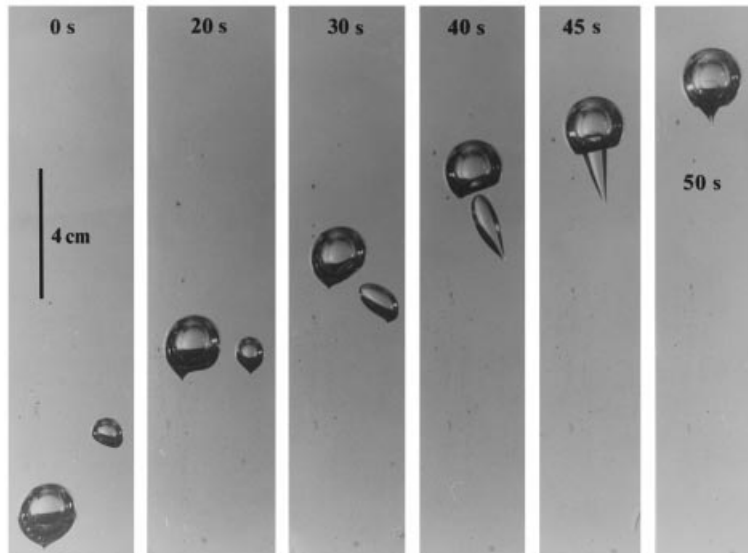
FIGURE 1. Interaction of two rising bubbles in corn syrup at $\mathscr{B} \approx 20$, showing cusp formation and entrainment of the smaller bubble in the rear of the larger one (from Manga 1997).

appears to be the most suitable for solving this class of problems. Axisymmetrical boundary-integral solutions have included the motion of a drop towards a solid wall or an interface (Chi & Leal 1989; Pozrikidis 1990*a*; Ascoli, Dandy & Leal 1990; Koch & Koch 1995; Manga & Stone 1995*a*), drop breakup in extensional flows (Stone & Leal 1989*a*,*b*), development of instabilities on a single drop in buoyancy-driven motion (Koh & Leal 1989; Pozrikidis 1990*b*), gravity-induced motion of two drops (Manga & Stone 1993), formation of satellite drops (Tjahjadi, Stone & Ottino 1992), deformation and the onset of breakup of contaminated drops (Stone & Leal 1990; Milliken, Stone & Leal 1993; Pawar & Stebe 1996) , and the thermocapillary migration of two drops (Zhou & Davis 1996). Most recently, axisymmetrical solutions have been applied to the cusp formation at a fluid interface (Pozrikidis 1998) and to study a rich variety of capture and breakup modes for two interacting drops settling under gravity (Davis 1999). Three-dimensional solutions have included steady-state deformation and the onset of breakup for a single drop in a shear flow (Rallison 1981), rheological calculations for a dilute emulsion in a shear flow (Kennedy, Pozrikidis & Skalak 1994), transient motion of ordered emulsions (Pozrikidis 1993), and the interaction of two or more drops (Manga & Stone 1995*b*; Manga 1997). Three-dimensional codes have also been developed to study the motion of several drops in a periodic cell subject to shear flow with rheological applications (Loewenberg & Hinch 1996), the self-diffusion due to hydrodynamical interactions in a dilute sheared emulsion (Loewenberg & Hinch 1997), pair interactions of drops/bubbles settling under gravity with deformation-induced capture and onset of breakup (Zinchenko, Rother & Davis 1997), the effect of surfactants on the rheology of dilute emulsions (Li & Pozrikidis 1997), and the motion of a periodic array of drops through a cylindrical tube (Coulliette & Pozrikidis 1998). Most recently, Cristini, Blawzdziewicz & Loewenberg (1998) developed a fully adaptive isotropic mesh algorithm and applied it to sample three-dimensional breakup calculations.

Accurate and robust three-dimensional boundary-integral simulation of deformable drops with arbitrary ratio of drop and medium viscosities, λ, remains a computationally intensive and problematic task, especially when complicated shapes and extreme cases are of interest. Our previous code (Zinchenko *et al.* 1997) for interacting drops incorporated some new ideas to overcome difficulties with the curvature calculation for unstructured surface triangulations, dynamical mesh degradation, and poor convergence of velocity iterations for nearly touching drops with extreme λ. The resulting code was universally applicable to drops falling under gravity or submerged in an ambient flow, and high accuracy could be easily achieved for smooth globular shapes with a modest aspect ratio. Difficulties remained, however, for extreme cases. First, apparent shape singularities with extremely high curvature may appear even for moderate Bond numbers, causing the algorithm to stall. The structure and development of cusps in various viscous flows has attracted considerable attention (Richardson 1968; Buckmaster 1972, 1973; Acrivos & Lo 1978; Hinch & Acrivos 1979; Sherwood 1981, 1984; Joseph *et al.* 1991; Jeong & Moffatt 1992; Pozrikidis 1997, 1998). The experiments reported by Manga & Stone (1993, 1995*b*) and Manga (1997) for two air bubbles in corn syrup give examples when apparent singularities form very early on bubble surfaces (see figure 1). Although it is important to understand the local structure of cusps and how they develop, a previously unmet goal of greater significance for practical applications is the ability to predict the drop motion after development of the cusp.

Breakup simulations present another difficulty for three-dimensional codes. If a mesh of triangles covering the surface is allowed to considerably stretch, which will always occur when the number of boundary elements remains fixed, the curvature calculation becomes ill-conditioned and the problem of mesh control is quite difficult. Although our previous code (Zinchenko *et al.* 1997) could detect the onset of breakup of the smaller drop due to interaction with a larger one in buoyancy-driven motion, it was not possible to proceed beyond the very beginning of the neck formation and resolve any details of the breakup.

In the present work, which builds on the ideas from our previous study (Zinchenko *et al.* 1997), a three-dimensional boundary-integral algorithm for interacting drops with extreme deformations is developed which is capable of handling cusped bubbles/drops and drops which are close to breaking. The method remains logically simple, since it still employs an unstructured mesh of triangles with a fixed number of boundary elements and fixed connections for each surface. The key idea is to use the curvatureless form of the inhomogeneous term in the boundary-integral equation. This form includes only the normal vectors, which are usually much less sensitive to discretization errors than is the curvature. Unlike the first version of the curvatureless method suggested in Zinchenko *et al.* (1997), which was essentially limited to $\lambda = 1$ and well-separated surfaces, the present code is for arbitrary viscosity ratios and also applicable for small surface separations. This improvement was achieved by a proper regularization and the solution of an auxiliary boundary-integral equation for each surface, when necessary (§ 2). The traditional boundary-integral form (with curvature) is able to handle shapes with point singularities, but fails for drops with line singularities (sharp edges), because of the concentrated capillary force inherent in these types of singularities; the occurrence of line singularities in three-dimensional problems is confirmed both by the photographs of Manga & Stone (1993, 1995*b*) and Manga (1997) for experiments with two bubbles at moderately high Bond numbers (see figure 1) and by our calculations (§ 6). In contrast to the classical formulation, the curvatureless form eliminates the contribution of the concentrated capillary force

and appears to be the only successful three-dimensional method for drops/bubbles with line singularities. Regardless of the type of the singularities, a boundary-integral formulation should be accompanied by some smoothing procedure with a negligible global effect, to make stability constraints acceptable and facilitate calculations for cusped drops/bubbles; a simple form of the smoothing mechanism, sufficient for treating singularities on a compact shape, is suggested in §3. In §4, a combined best-paraboloid, best-plane iterative method for the normal vector calculation is developed, which overcomes the difficulty of ill-conditioning of the best-paraboloid method (Zinchenko *et al.* 1997) for highly stretched meshes, and always gives convergent iterations. In §5, a special passive mesh stabilization method for large deformations is developed, which is a significant extension of our previous mesh stabilization technique (Zinchenko *et al.* 1997). The new method still uses a mesh with fixed topology, which has a fixed number of nodes with fixed connections, but is now capable of mesh control for drops with high aspect ratio approaching breakup, and is, to a reasonable extent, curvature-adaptive. A different method was recently described by Cristini *et al.* (1998). It employs isotropic, adaptive mesh restructuring into compact triangles, with an increasing number of boundary elements, as a drop stretches and breakup is approached.

Although the present code may be applicable to a number of problems, we consider here the buoyancy-driven motion of two drops/bubbles of different sizes at moderate and moderately high Bond numbers, as a continuation of our previous study (Zinchenko *et al.* 1997). In §6.1, the phenomenon of deformation-induced capture through coating or entrainment, discovered by Manga & Stone (1993) for two bubbles (see figure 1 for an illustration of entrainment), is considered, and the present code is used to systematically calculate the capture efficiency for $\lambda \ll 1$ as a function of the Bond number and size ratio. In §6.2, the three-dimensional breakup of the smaller drop due to hydrodynamical interaction with a larger one is considered; for $\lambda = O(1)$, this phenomenon is more typical than is deformation-induced capture. A combination of the curvatureless formulation (§2) and a new passive mesh stabilization technique (§5) allows the calculations to closely approach breakup and accurately predict by extrapolation both the breakup moment and the volume partition for Bond numbers which are moderately supercritical; under the same conditions, the traditional boundary-integral formulation fails at an early stage of the breakup simulation, if the mesh triangles are allowed to stretch. The present code is also used in §6.2 to study systematically the breakup efficiency, which is related to the maximum horizontal offset far upstream leading to breakup as a function of the Bond number and size ratio for $\lambda = 1$ and 2. An interesting phenomenon of combined capture and breakup, when the smaller drop starts breaking without being released from the dimple formed on the larger one, has been found and is discussed in §6.3. Finally, an attempt is made in §6.3 to classify all possible modes of two-drop interaction in buoyancy-driven motion for $\lambda = O(1)$. A detailed quantitative picture, however, would require additional calculations not attempted in the present work. Concluding remarks are presented in §7.

2. Curvatureless boundary-integral formulation

Consider, as a definite case, a system of N deformable drops of density ρ' and viscosity μ' settling in an unbounded quiescent medium of density ρ_e and viscosity μ_e at negligibly small Reynolds numbers. The traditional boundary-integral formulation (Rallison & Acrivos 1978; Pozrikidis 1992) gives a system of Fredholm second-kind

integral equations for the interfacial velocity $u(y)$:

$$u(y) = \frac{2(\lambda - 1)}{(\lambda + 1)} \sum_{\alpha=1}^{N} \int_{S_\alpha} u(x) \cdot T(x - y) \cdot n(x) \mathrm{d}S_x + F(y), \qquad (2.1)$$

where $\lambda = \mu'/\mu_e$ is the viscosity ratio,

$$T(r) = \frac{3}{4\pi} \frac{rrr}{r^5} \qquad (2.2)$$

is the stresslet corresponding to the free-space Green function

$$G(r) = -\frac{1}{8\pi} \left[\frac{I}{r} + \frac{rr}{r^3} \right], \qquad (2.3)$$

$n(x)$ is the outward unit normal at $x \in S_\alpha$, and the summation is over all drop surfaces S_α in the system. The inhomogeneous term is

$$F(y) = \frac{2}{\mu_e(\lambda + 1)} \sum_{\alpha=1}^{N} \int_{S_\alpha} \left[2\sigma k(x) + \left(\rho_e - \rho' \right) gz \right] n(x) \cdot G(x - y) \mathrm{d}S_x, \qquad (2.4)$$

where σ is the constant surface tension, $k(x) = \frac{1}{2}(k_1 + k_2)$ is the mean surface curvature at x, g is the gravity acceleration, and z is the Cartesian coordinate in the direction of gravity.

The curvature calculation on a triangulated surface is widely recognized as the main source of errors in three-dimensional numerical implementations of the boundary-integral method. We have found that our best paraboloid technique (Zinchenko *et al.* 1997), which is a development of Rallison's (1981) idea, provides a robust and accurate method to calculate the curvature on an unstructured mesh for generic smooth shapes with moderate and moderately large deformations. Difficulties occur, however, when the regions of extremely high curvature with $O(1)$ contributions to the boundary integral (2.4) develop. In this case, the inability to calculate the curvature near the apparent singularity causes a global numerical error in the vector field $F(y)$ and breakdown of the algorithm. Another example of difficulties is extreme drop elongation close to breakup, when the mesh of triangles becomes highly stretched and makes the best-paraboloid method ill-conditioned. The present work demonstrates that considerable progress in overcoming these difficulties can be made by using a new, *curvatureless* form of the inhomogeneous term (2.4). Unlike the first version of the curvatureless method (Zinchenko *et al.* 1997), which was limited to $\lambda = 1$ and well-separated surfaces, the present method described below is for arbitrary viscosity ratio λ and is also applicable for small surface separations.

The curvature contribution from each surface S_α to the integrals (2.4),

$$\Phi(y) = \int_{S_\alpha} k(x)n(x) \cdot G(x - y) \mathrm{d}S_x, \qquad (2.5)$$

can be transformed as (Zinchenko *et al.* 1997)

$$\Phi(y) = \frac{1}{16\pi} \int_{S_\alpha} \frac{r}{r^3} \left\{ 1 - \frac{3[r \cdot n(x)]^2}{r^2} \right\} \mathrm{d}S_x, \qquad (2.6)$$

with $r = x - y$. The difficulty is that the new form (2.6) is divergent when $y \in S_\alpha$ and should be taken as a principal-value integral, while the original form (2.5) could be calculated (for smooth shapes) as a regular integral for $y \in S_\alpha$ after singularity

subtraction (Pozrikidis 1992, p. 178). Because of the $O(r^{-2})$ singularity in the integrand, the new form (2.6) is also difficult to use for y close to S_α (which occurs for drops at small separation), while near-singularity subtraction (Loewenberg & Hinch 1996) could be used to handle (2.5) in this case.

It is possible, however, to first make the new form (2.6) non-singular for $y \in S_\alpha$ by considering the normal and tangential components of $\boldsymbol{\Phi}(y)$ separately. The normal component can be written as (Zinchenko *et al.* 1997)

$$\boldsymbol{\Phi}(y) \cdot \boldsymbol{n}(y) = \frac{1}{16\pi} \int_{S_\alpha} \frac{\boldsymbol{r} \cdot [\boldsymbol{n}(x) + \boldsymbol{n}(y)]}{r^3} \left\{ 1 - \frac{3[\boldsymbol{r} \cdot \boldsymbol{n}(x)][\boldsymbol{r} \cdot \boldsymbol{n}(y)]}{r^2} \right\} \mathrm{d}S_x, \qquad (2.7)$$

which is a regular integral since $\boldsymbol{r} \cdot [\boldsymbol{n}(x) + \boldsymbol{n}(y)] = O(r^3)$ for $x \to y \in S_\alpha$. To regularize the tangential component of (2.6), we note that

$$\frac{\boldsymbol{r} \times \boldsymbol{n}(y)}{r^3} \left\{ 1 - \frac{3[\boldsymbol{r} \cdot \boldsymbol{n}(x)]^2}{r^2} \right\}$$

$$= \frac{\boldsymbol{r} \times [\boldsymbol{n}(y) - \boldsymbol{n}(x)]}{r^3} - \frac{3[\boldsymbol{r} \times \boldsymbol{n}(y)][\boldsymbol{r} \cdot \boldsymbol{n}(x)]\{\boldsymbol{r} \cdot [\boldsymbol{n}(x) + \boldsymbol{n}(y)]\}}{r^5}$$

$$+ \boldsymbol{n}(x) \times \nabla_x \frac{1}{r} + 4\pi [\boldsymbol{n}(y) \cdot \boldsymbol{T}(x - y) \cdot \boldsymbol{n}(x)] \times \boldsymbol{n}(y). \qquad (2.8)$$

As follows from the integral identity for the double-layer kernal $\boldsymbol{T}$ (Pozrikidis 1992, p. 21), the last term of (2.8) does not contribute to the integral over S_α. The third term also does not contribute, since, using Gauss' theorem, its principal value can be replaced by the integral over a small hemisphere centred at $y \in S_\alpha$, and the latter integral vanishes. For this reason,

$$\boldsymbol{n}(y) \times \int_{S_\alpha} \frac{\boldsymbol{r} \times \boldsymbol{n}(y)}{r^3} \left\{ 1 - \frac{3[\boldsymbol{r} \cdot \boldsymbol{n}(x)]^2}{r^2} \right\} \mathrm{d}S_x$$

$$= \int_{S_\alpha} \boldsymbol{n}(y) \times \left\{ \frac{\boldsymbol{r} \times [\boldsymbol{n}(y) - \boldsymbol{n}(x)]}{r^3} - \frac{3[\boldsymbol{r} \times \boldsymbol{n}(y)][\boldsymbol{r} \cdot \boldsymbol{n}(x)]\{\boldsymbol{r} \cdot [\boldsymbol{n}(x) + \boldsymbol{n}(y)]\}}{r^5} \right\} \mathrm{d}S_x. \qquad (2.9)$$

The right-hand side of (2.9) is a regular integral, since

$$\boldsymbol{n}(y) \times \{\boldsymbol{r} \times [\boldsymbol{n}(y) - \boldsymbol{n}(x)]\}$$

$$= \{\boldsymbol{n}(y) \cdot [\boldsymbol{n}(x) - \boldsymbol{n}(y)]\}\boldsymbol{r} - [\boldsymbol{r} \cdot \boldsymbol{n}(y)][\boldsymbol{n}(x) - \boldsymbol{n}(y)] = O(r^3) \qquad (2.10)$$

at $x \to y \in S_\alpha$. By combining the results (2.7) and (2.9) for the normal and tangential components, the vector field (2.5) for $y \in S_\alpha$ can be represented as a *regular curvatureless integral*,

$$\boldsymbol{\Phi}(y)_{|S_\alpha} = \frac{1}{16\pi} \int_{S_\alpha} \left\{ [\boldsymbol{r} \cdot \boldsymbol{n}(x)]\boldsymbol{n}(y) + [\boldsymbol{r} \cdot \boldsymbol{n}(y)]\boldsymbol{n}(x) \right.$$

$$\left. + [1 - \boldsymbol{n}(x) \cdot \boldsymbol{n}(y)]\boldsymbol{r} - \frac{3\boldsymbol{r} \cdot [\boldsymbol{n}(x) + \boldsymbol{n}(y)][\boldsymbol{r} \cdot \boldsymbol{n}(x)]\boldsymbol{r}}{r^2} \right\} \frac{\mathrm{d}S_x}{r^3}, \qquad (2.11)$$

amenable for calculating $\boldsymbol{\Phi}(y)_{|S_\alpha}$.

For well-separated drops, the values of the vector field (2.5) outside S_α can be directly calculated from the curvatureless form (2.6). However, if there are surfaces close to S_α, the solution of an auxiliary integral equation is needed. Since the surface

tension force $2\sigma k\boldsymbol{n}$ has a zero rigid-body projection on S_α, i.e.

$$\int_{S_\alpha} k(\boldsymbol{x})\boldsymbol{n}(\boldsymbol{x})\mathrm{d}S_x = \int_{S_\alpha} \boldsymbol{x} \times k(\boldsymbol{x})\boldsymbol{n}(\boldsymbol{x})\mathrm{d}S_x = \boldsymbol{0}, \qquad (2.12)$$

$k(\boldsymbol{x})\boldsymbol{n}(\boldsymbol{x})$ can be represented as the boundary stress vector for some Stokes flow inside S_α. Hence, using the reciprocal identity, the vector field (2.5) outside S_α can be written as a double-layer potential:

$$\boldsymbol{\Phi}(\boldsymbol{y}) = 2\int_{S_\alpha} \boldsymbol{v}(\boldsymbol{x}) \cdot \boldsymbol{T}(\boldsymbol{x} - \boldsymbol{y}) \cdot \boldsymbol{n}(\boldsymbol{x})\mathrm{d}S_x, \qquad (2.13)$$

where the unknown density $\boldsymbol{v}(\boldsymbol{x})$ satisfies the boundary-integral equation

$$\boldsymbol{v}(\boldsymbol{y}) = 2\int_{S_\alpha} \boldsymbol{v}(\boldsymbol{x}) \cdot \boldsymbol{T}(\boldsymbol{x} - \boldsymbol{y}) \cdot \boldsymbol{n}(\boldsymbol{x})\mathrm{d}S_x - \boldsymbol{\Phi}(\boldsymbol{y}), \quad \boldsymbol{y} \in S_\alpha. \qquad (2.14)$$

It follows from (2.5) and (2.14) that

$$2\int_{S_\alpha} \boldsymbol{v}(\boldsymbol{y}) \cdot \boldsymbol{n}(\boldsymbol{y})\mathrm{d}S_y = -\int_{S_\alpha} \boldsymbol{\Phi}(\boldsymbol{y}) \cdot \boldsymbol{n}(\boldsymbol{y})\mathrm{d}S_y = 0. \qquad (2.15)$$

The solution of (2.14) is determined to within an arbitrary rigid-body motion. Using (2.15), Wielandt's deflation, and singularity subtraction (Pozrikidis 1992), equation (2.14) can be rewritten as

$$\boldsymbol{v}(\boldsymbol{y}) = 2\int_{S_\alpha} [\boldsymbol{v}(\boldsymbol{x}) - \boldsymbol{v}(\boldsymbol{y})] \cdot \boldsymbol{T}(\boldsymbol{x} - \boldsymbol{y}) \cdot \boldsymbol{n}(\boldsymbol{x})\mathrm{d}S_x + \boldsymbol{v}(\boldsymbol{y}) - \boldsymbol{v}'(\boldsymbol{y})$$
$$+ \frac{\boldsymbol{n}(\boldsymbol{y})}{S_\alpha} \int_{S_\alpha} \boldsymbol{v}(\boldsymbol{x}) \cdot \boldsymbol{n}(\boldsymbol{x})\mathrm{d}S_x - \boldsymbol{\Phi}(\boldsymbol{y}), \quad \boldsymbol{y} \in S_\alpha \qquad (2.16)$$

(a convenient expression for the rigid-body projection $\boldsymbol{v}'(\boldsymbol{y})$ is given by (11)–(15) of Zinchenko *et al.* 1997). Equation (2.16) has a spectral radius less than unity, and its unique solution can be found by simple iterations of the left-hand side. Once the density $\boldsymbol{v}(\boldsymbol{x})$ has been determined, $\boldsymbol{\Phi}(\boldsymbol{y})$ can be calculated in the vicinity of S_α by the double-layer potential (2.13), with near-singularity subtraction (Loewenberg & Hinch 1996) used to considerably improve the accuracy:

$$\boldsymbol{\Phi}(\boldsymbol{y}) = 2\int_{S_\alpha} [\boldsymbol{v}(\boldsymbol{x}) - \boldsymbol{v}(\boldsymbol{x}^*)] \cdot \boldsymbol{T}(\boldsymbol{x} - \boldsymbol{y}) \cdot \boldsymbol{n}(\boldsymbol{x})\mathrm{d}S_x, \qquad (2.17)$$

where $\boldsymbol{x}^*$ is the collocation node on S_α that is nearest to $\boldsymbol{y}$.

Thus, the proposed method allows calculation of the inhomogeneous term (2.4) for arbitrary viscosity ratios and separations using only the normal vectors $\boldsymbol{n}(\boldsymbol{x})$. It is fortunate that the solutions of (2.16), when necessary, are independent for the different drop surfaces, and so their cost is at most $O(M^2N)$ per iteration, where M is the number of collocation nodes per drop, compared to $O(M^2N^2)$ for the principal equation (2.1). For this reason, the solutions of (2.16) usually do not noticeably slow down the whole calculation, even for $N = 2$ considered in the present work. Difficulties may arise, however, when the drop surfaces are close together (so that the solution of (2.16) is needed) and S_α has a high aspect ratio. In this case, simple iterations for (2.16) may be poorly convergent. Biconjugate gradient iterations, which are discussed in Zinchenko *et al.* (1997), largely overcome this difficulty.

3. Dynamical smoothing of cusp singularities

A substantial difficulty with boundary-integral calculations for deformable drops/ bubbles at moderate and large but finite capillary or Bond numbers is the development of apparent shape singularities, especially for $\lambda \ll 1$, causing breakdowns in straightforward numerical algorithms. These apparent singularities have been observed in many experiments (e.g. Joseph *et al.* 1991; Manga & Stone 1993), and their local structure has attracted considerable attention. Richardson (1968) showed that the only possible singularity on a free surface in two dimensions is a genuine cusp. Joseph *et al.* (1991) analysed the local asymptotic shape structure $y = -cx^{3/2}$ of this cusp, neglecting surface tension. Neither of the solutions of Richardson (1968) and Joseph *et al.* (1991) describe the vicinity of the tip. By the exact solution of a specific, two-dimensional free-surface problem, Jeong & Moffatt (1992) demonstrated that the classical continuum formulation remains mathematically consistent at the tip, and a finite surface tension acts to smooth the cusp; however, the smoothing radius, scaled with the characteristic length of the problem, was found to be $\sim \exp(-32\pi Ca)$, which is on the order of molecular scale even for a modest capillary number of $Ca \approx 0.25$. This explains why two-dimensional cusps appear to look like true singularities, as well as exhibit a sharp transition from smooth to cusped shapes, as the capillary number is increased. In the axisymmetrical case, when the apparent singularity is formed at a single point, the local shape at the tip is cone-like, rather than cusp-like (Buckmaster 1972, 1973; Acrivos & Lo 1978; Sherwood 1981, 1984); a small three-dimensional perturbation (Hinch & Acrivos 1979) does not seem to change this conclusion. Again, these solutions are inapplicable at the very tip, where a transition to cusping and then to a rounded end is believed to occur (Buckmaster 1972, 1973; Sherwood 1981, 1984). However, a local analysis, which would have demonstrated smoothing by surface tension, remains an outstanding problem for a point singularity.

In the present work, we have not attempted to contribute to understanding the local structure of the apparent singularities, despite the importance of this issue. Rather, we are interested in a robust three-dimensional boundary-integral algorithm for deformable drops/bubbles, which would allow global calculations to continue after cusp development. To our knowledge, no attempts have been reported to solve this problem. Noh, Kang & Leal (1993) discussed the difficulty of obtaining a global axisymmetrical numerical solution for a single cusped bubble in a non-Newtonian fluid. Pozrikidis (1990) and Manga & Stone (1993) successfully made axisymmetric long-time simulations for drops with shape irregularities, but mostly for zero surface tension and not including the extreme case $\lambda \ll 1$. Pozrikidis (1997, 1998) has recently studied the development of singularities in various two-dimensional and axisymmetrical flows and found, unexpectedly, that replacing bubbles with drops having $\lambda = O(1)$ does not necessarily have a smoothing effect; however, the evolution after cusp formation in essentially unsteady flows was not his goal.

Figure 1, showing photos from Manga (1997) of two bubbles rising under buoyancy, illustrates the challenge of the task undertaken in the present work. In these photos, singularities form very early on the bubble surfaces, and, to be conclusive in determining the further motion, a boundary-integral algorithm would have to be able to handle cusped shapes. When an apparent singularity forms, a straightforward boundary-integral code breaks down due to prohibitive numerical stiffness and other reasons. To proceed, the singularity must be smoothed. Natural smoothing by surface tension gives an extremely high curvature, far beyond the resolution of any global numerical method, and is of no help. Instead, the idea of our approach is to introduce an artificial, well-controlled mechanism of small *dynamical smoothing* which

prevents shape irregularities from forming. This turns out to be non-trivial, because the loss of smoothness is not a numerical artifact, and several natural remedies that we have attempted (such as adding small artificial terms to the boundary-integral equation) failed to prevent the development of apparent singularities. We have found that progress can instead be made when an artificial normal velocity is added to that obtained from the boundary-integral solution at each time step. This additional velocity is on the order of $\epsilon \ll 1$ on the smooth part of the bubble (or drop), but somewhat higher in the singularity region, and, when properly constructed (see below), pulls the cusp in, thus not allowing catastrophically high curvature to develop and facilitating long-time calculations. The limit $\epsilon \to 0$ can then be taken, simultaneously with increasing the number N_Δ of triangular elements per drop, to produce convergent results for global motion for line as well as point singularities, with increasingly sharp singularities. For realistic triangulations and supercritical Bond numbers, when the singularity in the exact solution is quite sharp on the drop lengthscale, it is not reasonable to expect convergent results with this procedure in the cusp region, but this is not necessary (see §6.1) if only global motion is the goal.

For the cusp-smoothing procedure to correctly predict the global motion for line as well as point singularities, the use of the curvatureless formulation of §2 is essential. Indeed, if the developed singularity is a two-dimensional cusp, with extremely high curvature along a line, a concentrated capillary force will be generated (cf. Richardson 1968). Namely, the integral of $k\boldsymbol{n}$ over the crest area in (2.5) is $O(1)$, thus making a numerically unresolvable $O(1)$ error in the field $\boldsymbol{\Phi}(\boldsymbol{y})$ *away* from the crest. For this reason, the conventional boundary-integral formulation fails to continue the calculation beyond the singularity formation (unless extremely crude smoothing is used, leading to erroneous results). In contrast, in the curvatureless formulation (2.6), the crest area has a *zero* contribution to the field $\boldsymbol{\Phi}(\boldsymbol{y})$ away from the crest. Owing to this, a small dynamical smoothing, which is necessary to facilitate the use of the regularized form (2.11) and make stability constraints acceptable, does not have a global effect, and the calculations can be successfully continued after the apparent singularity development (§6.1). In the case of a point singularity, the conventional formulation (2.5) in combination with dynamical smoothing is successful, but the curvatureless form (2.6) is still advantageous. Indeed, the contribution of the cusp region to $\boldsymbol{\Phi}(\boldsymbol{y})$ away from the cusp is $O(r)$ for (2.5) and much smaller, $O(r^2)$, for (2.6), where r is the characteristic radius of curvature at the tip after smoothing. Although it would seem attractive to use the conventional formulation and contour integration for $k\boldsymbol{n}$ to tackle the problem of apparent singularities, we have been unable to make this alternative successful, probably due to general difficulties associated with the contour integration method (Zinchenko *et al.* 1997).

The above arguments showing that detailed resolution of the cusp region can always be avoided in the calculation of the global motion when the curvatureless form is used also indicate that additional physical mechanisms should not have a global effect, if they invalidate the classical model in the small cusp region only. For example, in practice, tip streaming often occurs for $\lambda \ll 1$, which is mostly attributed to surfactant effects (de Bruijn 1993; Stone 1994). Even small amounts of surfactants accumulating in the tip region can strongly reduce the surface tension there (Milliken *et al.* 1993; Pawar & Stebe 1996), making the pointed end even sharper and causing tip streaming, until the surfactant is swept away (de Bruijn 1993). However, the associated mass flow from the tip is normally very small (Sherwood 1984) and should not change appreciably the overall surface dynamics, at least on the typical timescale of interest and for capillary or Bond numbers which are only modestly supercritical; otherwise, it would be difficult

to explain the agreement between experiments and the two-dimensional, very high-resolution calculations of Palmquist & Kistler (unpublished), based on the classical model for supercritical conditions (see Joseph & Renardy 1993 for this comparison).

There are various relations which may be chosen for the additional normal smoothing field. Among several possibilities tested, we have found it best to modify the normal velocity $q_i = \boldsymbol{u}_i \cdot \boldsymbol{n}_i$, where the subscript refers to node i, from the boundary-integral solution to

$$q_i + \langle q \rangle_\alpha \left\{ 1 - \exp \left[\epsilon_\alpha \left(\frac{K_i}{\langle K \rangle_\alpha} - 1 \right)^2 \right] \right\}, \tag{3.1}$$

where $\epsilon_\alpha \ll 1$ is the smoothing parameter for surface S_α,

$$K = \left[(k_1^2 + k_2^2)/2 \right]^{1/2} \tag{3.2}$$

is a measure of the local curvature (note that $K = k$ for a sphere), and $\langle q \rangle_\alpha$ and $\langle K \rangle_\alpha$ are the average values of $|q|$ and K over S_α. In addition, an appropriate small constant is added to (3.1) to make zero the total flux through S_α (when $\epsilon_\alpha \neq 0$). On the main, smooth part of the drop or bubble, the modification to the normal velocity from (3.1) is very small, of order $\epsilon_\alpha \langle q \rangle_\alpha$ (or even smaller, if the surface is nearly spherical as is often the case in bubble cusping). In the cusp region, however, where K may attain high values, (3.1) gives a stronger negative correction to the normal velocity, which pulls the cusp in, and the exponential dependence does not allow catastrophically high curvature to develop. In the limit $\epsilon \to 0$, $N_\Delta \to \infty$, global characteristics are independent of the relation between ϵ and N_Δ (§ 6.1), suggesting that the choice of (3.1) is purely technical. The form of the smoothing relation only affects the convergence rate. The principal curvatures k_1 and k_2 for (3.1)–(3.2) are calculated by the method of § 4 and do not have to be accurate, and so the method remains effectively curvatureless. Besides, apparent singularities typically develop for low-aspect-ratio shapes, when mesh triangles remain compact, and the curvature calculation on the smooth part of the surface then proceeds without difficulties.

Kelmanson (1983 a, b) has developed an elegant method for two-dimensional Stokes flows past solid boundaries with sharp corners, which effectively subtracts out the analytical behaviour in the corner region from the boundary-integral equation and dramatically improves the convergence. Unfortunately, we have been unable to develop a similar approach in the present work because (i) the flow is three-dimensional, (ii) the location and type of the singularity are not known *a priori*, (iii) it is not clear how to switch from the regime with smooth surfaces to cusping, and (iv) the available analytic information about the singularity structure is incomplete. This inability to use the local singularity structure results in a modest rate of convergence, when cusps are present (§ 6.1). Finally, it should be noted that the combination of (3.1) with the curvatureless formulation provides a successful method when a cusp develops on a compact shape, which is often the case for bubbles at moderate Bond numbers. In a less typical case, when a singularity develops on a high aspect ratio drop, a satisfactory method has yet to be developed.

4. Combined best-paraboloid, best-plane strategy for the curvature and normal vector calculations

The algorithm of fitting the best paraboloid (Zinchenko *et al.* 1997) for the normal vector $\boldsymbol{n}(\boldsymbol{x}_i)$ and mean curvature $k(\boldsymbol{x}_i)$ calculation at a vertex $\boldsymbol{x}_i$ of an unstructured
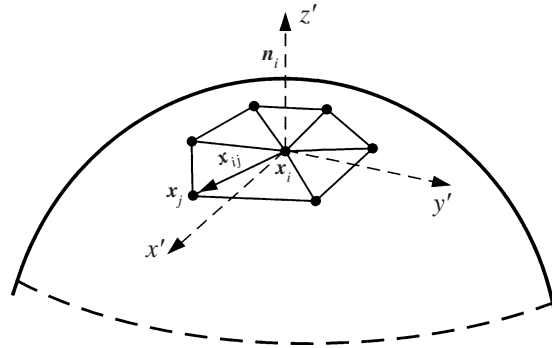
FIGURE 2. Schematic for the calculation of the mean curvature and normal vector at node x_i of a triangulated surface, for the typical coordination number of six.

mesh of triangles (figure 2) is based on the following idea. If the z'-axis of the local Cartesian coordinates (x', y', z') with the origin x_i was directed along the normal vector $n(x_i)$, then z' as a quadratic function of x' and y' would be a good local representation for any smooth surface. However, $n(x_i)$ is not known *a priori*, and iterations are needed. First, a paraboloid is found with a chosen direction of the z'-axis, which passes through x_i and fits best its neighbours by the least-squares method. The unit normal to this paraboloid at x_i is used as the new direction of the z'-axis, and the procedure is repeated until the convergence is reached. Then, $n(x_i)$ and $k(x_i)$ are taken as the corresponding quantities for the fitted paraboloid. This method was found to be robust and more accurate than the other local methods tested (Zinchenko *et al.* 1997), and non-convergence of iterations was never observed for generic smooth shapes with moderate and moderately large deformations. However, our more recent tests for highly stretched ellipsoids ($a = 1$, $b = 0.2$, $c = 0.1$) show divergence of this iterative procedure for several points, if the number of triangular elements is less than about 1000. This divergence is removed, however, for finer triangulations. Non-convergence of iterations is more often observed in real boundary-integral calculations, when a drop reaches a very high aspect ratio, especially in cases of mesh irregularity due to drop stretching and the three-dimensional character of the motion. Even if the best paraboloid is found by convergent iterations, another potential problem for highly stretched shapes with some mesh irregularity may be ill-conditioning of the procedure. The surface triangulations we work with are initially obtained in a standard way from regular polyhedra by a series of refinements, as discussed by Zinchenko *et al.* (1997). In this case, the coordination number is 5 or 6, i.e. always enough to construct a local paraboloid. However, if the mesh becomes highly stretched, some neighbours of x_i tend to merge, making the effective coordination number less than 5 (E. J. Hinch, personal communication) and potentially causing ill-conditioning. Since extreme deformations are of primary interest for the present work, the best-paraboloid technique was modified as follows, to overcome these shortcomings.

First, instead of a paraboloid, the best plane is initially constructed for vertex x_i. This plane passes through x_i, and its unit normal, $n^*(x_i)$, provides a minimum to the function

$$\sum_{j \in \mathscr{A}_i} \frac{(x_{ij} \cdot n^*)^2}{||x_{ij}||^2}. \tag{4.1}$$

Here the summation is over the set $\mathscr{A}_i$ of nodes j adjacent to node i, and $x_{ij} = x_j - x_i$

are the vectors from x_i to its neighbours. To find n^* efficiently, the characteristic equation

$$\det(A - \mu I) = 0, \quad A = \sum_{j \in \mathscr{A}_i} \frac{x_{ij} x_{ij}}{||x_{ij}||^2}, \tag{4.2}$$

is solved first, using Newton's method to find the minimum positive root μ (starting from $\mu = 0$ is always appropriate), and n^* is then found as the eigensolution of

$$(A - \mu I) \cdot n^* = 0 \tag{4.3}$$

with an appropriate sign. Since only two neighbours are enough to construct the best plane, determining n^* is a well-posed problem for all cases of interest. Using n^* as a unit normal to the surface in the curvatureless formulation gives a robust code, but may be too crude.

To find a generally better approximation n to the surface normal at x_i, consider a local coordinate system (x', y', z') centred at x_i and the z'-axis along n (figure 2). Let x'_{ij}, y'_{ij}, z'_{ij} be the (x', y', z') components of the vector x_{ij} and

$$F(n) = \min_{C,D,E} \sum_{j \in \mathscr{A}_i} \frac{(Cx'^2_{ij} + Dx'_{ij}y'_{ij} + Ey'^2_{ij} - z'_{ij})^2}{||x_{ij}||^2} \tag{4.4}$$

be a measure of the local deviation of the surface from the best paraboloid $z' = Cx'^2 + Dx'y' + Ey'^2$ with the given axes x', y', z'. The minimum (4.4) is found by a simple solution of a linear system for C, D, and E, and is independent of an arbitrary rotation of the (x', y', z') system about the z'-axis. Finally, the normal vector n is required to provide a minimum to the function

$$F(n) + \gamma ||n - n^*||^4 \tag{4.5}$$

under the constraint $||n|| = 1$, where γ is a fixed coefficient of $O(1)$. The required minimization is obtained by gradient iterations, as described in Appendix A. If n is the exact surface normal and the mesh is regular, $F(n)$ is $O(h^4)$, where h is the characteristic mesh size. Formally, the best-plane normal n^* is $O(h)$-accurate, and so the second term in (4.5) is also $O(h^4)$. In practice, however, the convergence of n^* to the exact normal is faster in a wide range of the number of collocation nodes on the drop, M, and the effect of the last term in (4.5) quickly disappears for fine regular triangulations. On the other hand, for meshes with irregularity, when the best-paraboloid procedure may be ill-conditioned, the last term in (4.5) does not allow n to deviate much from the crude approximation n^*.

Unlike the best-paraboloid iterations of Zinchenko *et al.* (1997), which may be occasionally divergent in extreme cases (see above), the gradient iterations (Appendix A) always converge (unless there is an exact mesh degeneration), both for $\gamma = 0$ and $\gamma \neq 0$ in (4.5). When convergent, the previous method gives the same normal vector and curvature as does the present method in the extreme case $\gamma = 0$ for the same triangulation. Besides, in the limit of fine triangulations, the convergence of the curvature and normal found by minimizing (4.5) to the exact values is always observed, both for $\gamma = 0$ and $\gamma \neq 0$. Thus, occasional divergence of our old iterations in extreme cases is by no means the divergence of the best-paraboloid method.

Figures 3 and 4 demonstrate the effect of γ on the accuracy of the normal vector and curvature calculations for an elongated axisymmetrical spool-like shape obtained by rotating the curve

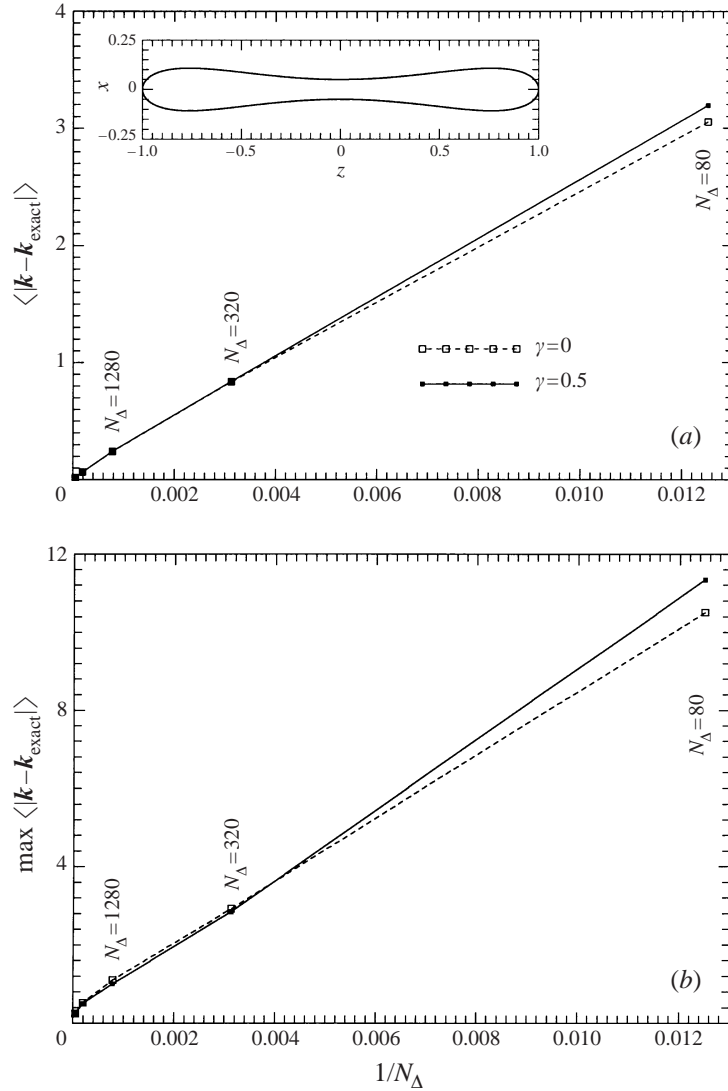$$x^2 = (0.2z^2 + 0.05)^2 (1 - z^2) \tag{4.6}$$

FIGURE 3. The average (*a*) and maximum (*b*) absolute errors $|k - k_{\text{exact}}|$ in the mean curvature calculation by the combined best-paraboloid, best-plane method for an axisymmetrical spool-like shape described by equation (4.6) and a different number N_Δ of triangular elements; the limit $\gamma = 0$ corresponds to the best-paraboloid method.

about the z-axis. To generate surface triangulations into $N_\Delta = 80$ to $20\,480$ elements, we took unit sphere triangulations prepared by a standard refinement procedure (e.g. Zinchenko *et al.* 1997) subject to a random rotation. Such a rotation may slow down the convergence, but was used for generality. These triangulations are then contracted along x- and y-axes by the factor $0.2z^2 + 0.05$, according to (4.6). As follows from (4.5), $\gamma \to \infty$ in figure 4 corresponds to the best-plane approximation $\boldsymbol{n}^*$, which is less crude than expected. No divergence of our old best-paraboloid iterations was detected in this test. As figures 3 and 4 show, the presence of γ in (4.5) may deteriorate the accuracy, but only for very crude regular triangulations; as the number of triangles grows, the effect of γ quickly disappears. Similar conclusions were drawn for highly stretched
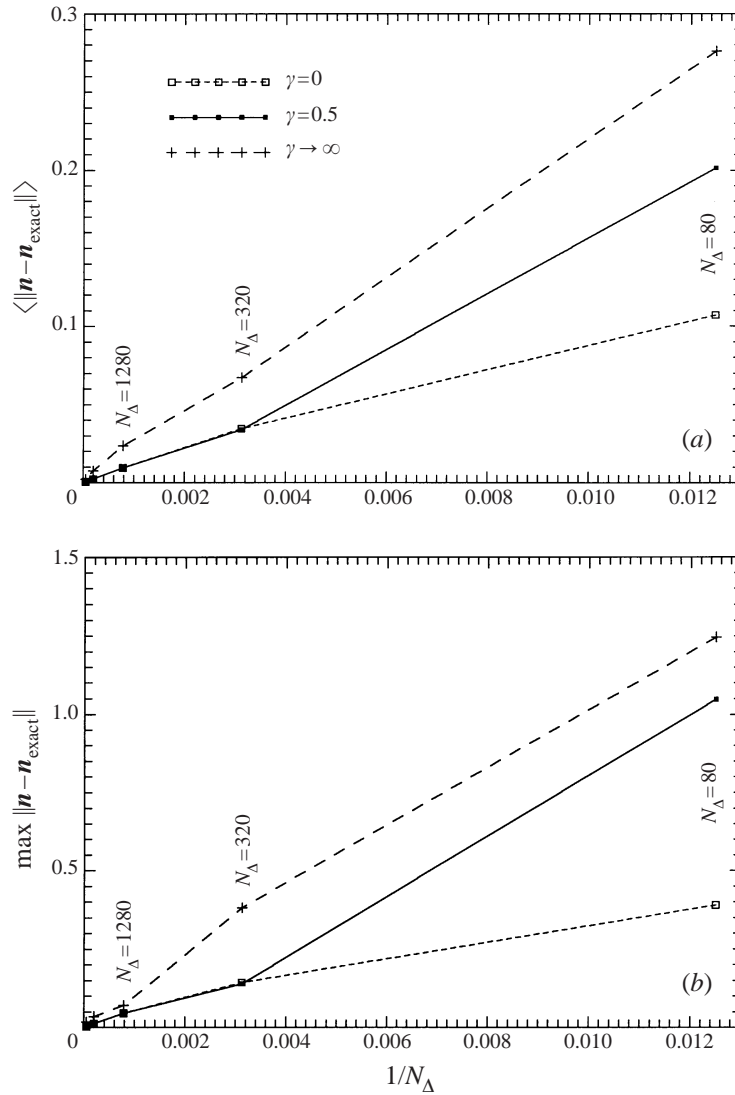
FIGURE 4. The average (*a*) and maximum (*b*) absolute errors $||\boldsymbol{n} - \boldsymbol{n}_{\text{exact}}||$ in the normal vector calculation by the combined best-paraboloid, best-plane method for an axisymmetrical spool-like shape (figure 3*a*) and a different number N_Δ of triangular elements. The limiting cases $\gamma = 0$ and $\gamma \to \infty$ correspond to the best-paraboloid and best-plane methods, respectively.

three-dimensional ellipsoids. Nevertheless, we prefer to retain the last term in (4.5) with $\gamma = 0.5$ in real boundary-integral calculations, to avoid ill-conditioning in extreme cases. If, for example, only four neighbours of each node had been used in this test, the best-paraboloid method ($\gamma = 0$) is not applicable; however, the combined procedure (4.5) with $\gamma = 0.5$ gives the normal vector $\boldsymbol{n}$ with about the same accuracy as $\boldsymbol{n}^*$.

We have also developed an alternative code for calculating geometric charac-teristics, which will be analysed elsewhere and is based on a combination of our best-paraboloid method (Zinchenko *et al.* 1997) and the concept of splines, so that global iterations are performed over the entire surface. For smooth generic shapes, with moderate and moderately large deformations, this method did not show appre-

ciable improvement of the curvature calculation, compared to the best-paraboloid method, but gave much more accurate normal vectors (which would be advantageous in the curvatureless algorithm). Unfortunately, we have found that, in extreme cases with cusped interfaces or highly elongated drops close to breakup, this method may be quite unreliable. For this reason, in the present work where extreme deformations are of interest, we have preferred the more robust scheme based on minimizing (4.5). It appears that, to be successful in extreme cases, a three-dimensional method for geometric characteristics should remain local.

5. Passive mesh stabilization for large deformations

A familiar difficulty in three-dimensional boundary-integral calculations for deformable drops is efficient mesh control. Namely, if the collocation nodes are simply advected with the fluid velocity or with the surface normal velocity, an initially regular unstructured mesh of triangles covering the surface becomes highly irregular after a short simulation time, thus invalidating the calculation. This loss of regularity, however, can be prevented by an additional tangential field. In the simplest version of the local grid tension method, internode springs are used to resist the mesh distortion, which often produces numerical stiffness with severe limitations on the time step. In contrast, the passive mesh stabilization method of Zinchenko *et al.* (1997) constructs the tangential field globally to minimize, on average, the rates of change of the distances between neighbouring nodes. This optimization problem is solved separately for each surface S_α. At any instant in time, the vertex velocities $V_i = \mathrm{d}x_i/\mathrm{d}t$ to be used in the shape updates are required to provide a minimum to the function

$$F(V_1, V_2, \ldots V_M) = \sum_{(i,j)} \left[\frac{\mathrm{d}}{\mathrm{d}t} ||x_{ij}||^2 \right]^2 = 4 \sum_{(i,j)} \left[x_{ij} \cdot (V_j - V_i) \right]^2, \tag{5.1}$$

where M is the number of vertices on S_α, and the summation is over all triangle edges (i, j) on S_α under the constraints

$$V_i \cdot n_i = q_i, \tag{5.2}$$

with the normal velocities $q_i = u_i \cdot n_i$ given by the solution of the boundary-integral equations. This simple method was found to be very robust for compact shapes, with soft stability limitations on the time step. Difficulties arise, however, for drops with high aspect ratio, when some mesh triangles tend to degenerate into line segments (note the darkened areas in figure 17 of Zinchenko *et al.* (1997) at $t = 5$ and 5.5), and there is no mesh adaptivity to high curvature at the tip (Zinchenko *et al.* 1997).

In the present work, we have developed a new version of passive mesh stabilization, which still uses a mesh with fixed connections and a fixed number of boundary elements, but is capable of mesh control for drops with high aspect ratio approaching breakup. Instead of (5.1), the function to minimize at each time step is

$$F = \sum_{(i,j)} \frac{1}{||x_{ij}||^4} \left[\frac{\mathrm{d}}{\mathrm{d}t} \left(x_{ij} \cdot (n_j^* - n_i^*) \right) \right]^2 \tag{5.3a}$$

$$+ c_1 \sum_{(i,j)} \frac{\Psi_i + \Psi_j}{||x_{ij}||^4} \left[\frac{\mathrm{d}}{\mathrm{d}t} ||x_{ij}||^2 \right]^2 \tag{5.3b}$$

$$+ c_2 \sum_{\Delta} \frac{\Psi_\Delta}{Q_\Delta^2} \left(\frac{\mathrm{d}Q_\Delta}{\mathrm{d}t} \right)^2. \tag{5.3c}$$

Each part of (5.3) is a result of considerable experimenting, and the chosen form requires some explanation.

In (5.3*a*) and (5.3*b*), the summation is over all mesh edges (i, j) on S_α, with $i < j$ to avoid double counting, $\mathbf{n}_i^*$ is the unit normal at vertex $\mathbf{x}_i$ calculated by the best-plane technique (§ 4),

$$\Psi_i = k_{\max}^2(i) - k_{\min}^2(i) + \frac{1}{a^2}, \tag{5.4}$$

where $k_{\max}(i)$ and $k_{\min}(i)$ are the estimations of the maximum and minimum curvatures at node $\mathbf{x}_i$ (see below), a is the radius of an equivalent sphere with the same volume as drop α, and c_1 is an $O(1)$ numerical factor. When the mesh is highly stretched, accurate curvatures may be unavailable, but they are not necessary in the curvatureless formulation. However, the following estimates through the normal vector variation between $\mathbf{x}_i$ and its neighbours suffice for (5.4):

$$k_{\max}^2(i) \approx \max_{j \in \mathscr{A}_i} \frac{||\mathbf{n}_j^* - \mathbf{n}_i^*||^2}{||\mathbf{x}_{ij}||^2}, \quad k_{\min}^2(i) \approx \min_{j \in \mathscr{A}_i} \frac{||\mathbf{n}_j^* - \mathbf{n}_i^*||^2}{||\mathbf{x}_{ij}||^2}. \tag{5.5}$$

Obviously, $\mathbf{x}_{ij} \cdot (\mathbf{n}_j^* - \mathbf{n}_i^*)$ is a measure of the surface variation in the direction of the edge $\mathbf{x}_{ij}$, and so the first term of F, (5.3*a*), acts to anisotropically adapt the mesh to high curvature, which is important to produce enough resolution at the drop tips. Indeed, initially, when the drop is spherical, all $\mathbf{x}_{ij} \cdot (\mathbf{n}_j^* - \mathbf{n}_i^*)$ are almost the same, and so a small time change of $\mathbf{x}_{ij} \cdot (\mathbf{n}_j^* - \mathbf{n}_i^*)$ will result in anisotropic mesh adaptation; namely, if the curvature in the direction of the edge $\mathbf{x}_{ij}$ is high, this edge will tend to be shorter, and vice versa. In some problems, it is useful to increase the adaptivity and replace the term under summation (5.3*a*) by $||\mathbf{x}_{ij}||^{-2}\{d[\mathbf{x}_{ij} \cdot (\mathbf{n}_j^* - \mathbf{n}_i^*)/||\mathbf{x}_{ij}||]/dt\}^2$, but the form (5.3*a*) was chosen in the present work as the one with the better overall performance. Term (5.3*a*) alone would cause instability in case of a nearly flat spot on a drop, with $k \approx 0$, which occurs often in boundary-integral calculations. This fault is corrected by the second term, (5.3*b*), which has a structure similar to the non-adaptive function (5.1) and prevents the edges with low $\mathbf{x}_{ij} \cdot (\mathbf{n}_j^* - \mathbf{n}_i^*)$ from excessive elongation. Besides, the use of variable weights $\Psi_i + \Psi_j$ in (5.3*b*) plays an important role at the end of breakup simulations, causing slow migration of the collocation nodes from the ends to the neck region, where the weights $\Psi_i + \Psi_j$ are high, thus increasing the stability of the calculation.

In (5.3*c*), the summation is over all mesh triangles Δ on S_α, Ψ_Δ is the average of Ψ_i over the vertices i of Δ, c_2 is another $O(1)$ numerical factor, and

$$Q_\Delta = \sin^2 \alpha_1 + \sin^2 \alpha_2 + \sin^2 \alpha_3 \tag{5.6}$$

is the quality function for the mesh triangle Δ with the angles α_1, α_2 and α_3. Term (5.3*c*) is vital for highly elongated shapes, since it acts to prevent mesh triangle degenerations and mesh 'wrinkles' by not allowing Q_Δ to become too small. Note that highly stretched, nearly isosceles triangles with the short side across the direction of the maximum drop elongation are allowed to form in regions where drops are significantly elongated. Unlike some high-aspect-ratio elements, these are not considered undesirable, since their quality value $Q_\Delta \approx 2$ is close to $Q_\Delta = 2.25$ for equilateral triangles; any method using a mesh with fixed topology would have to admit these elongated triangles in simulations for high-aspect-ratio drops. The form (5.3*c*) only resists the formation of obtuse mesh triangles with an angle close to π and a low quality value Q_Δ. The importance of using the quality function Q_Δ, instead of, for example, the triangle area, for more successful breakup simulations is further stressed in § 6.2.

As in (5.3b), the weights Ψ_Δ give the priority to the mesh control in higher-curvature zones. After experimenting with different test cases, we set $c_1 = 0.25$ and $c_2 = 2$ in (5.3) to provide a balance of mesh stabilization in the neck region and on the rest of the surface. The function F can be expressed in terms of the node velocities V_i and minimized under the constraints (5.2) by conjugate gradient iterations (see Appendix B for details).

If only moderately large deformations are of interest, an alternative form of the minimizing function can be used:

$$F = \sum_{(i,j)} \frac{1}{||\boldsymbol{x}_{ij}||^4} \left[\frac{\mathrm{d}}{\mathrm{d}t} \boldsymbol{x}_{ij} \cdot (\boldsymbol{n}_j^* - \boldsymbol{n}_i^*) \right]^2 \tag{5.7a}$$

$$+ c_1 \langle |k_{\max}| \rangle^2 \sum_{(i,j)} \frac{1}{||\boldsymbol{x}_{ij}||^4} \left[\frac{\mathrm{d}}{\mathrm{d}t} ||\boldsymbol{x}_{ij}||^2 \right]^2 \tag{5.7b}$$

$$+ c_2 \langle |k_{\max}| \rangle^2 \sum_{\Delta} \frac{1}{S_\Delta^2} \left(\frac{\mathrm{d}S_\Delta}{\mathrm{d}t} \right)^2 . \tag{5.7c}$$

The only differences in (5.7) from (5.3) are the use of the average curvature $\langle |k_{\max}| \rangle$ over the entire surface, where $|k_{\max}|$ is given by (5.5), to weight (5.7b) and (5.7c), and the use of the mesh triangle area S_Δ in (5.7c) instead of the quality function; numerical implementation remains practically the same as for (5.3). Both modifications decrease the numerical stability in the neck region, and the form (5.7) cannot proceed as far as (5.3) in breakup simulations. On the other hand, (5.7), where applicable, typically describes drop elongation more accurately than does (5.3). The recommended values of the parameters in (5.7) are $c_1 = 0.25$ and $c_2 = 0.5$.

There also exists a very different approach to mesh control/adaptation, based on the idea of dynamical restructuring and suggested in its initial form by Unverdi & Tryggvason (1992). In this approach, compact mesh triangles are used and new collocation nodes must be added as a drop elongates, while the present method operates with a stretched mesh and a fixed number of boundary elements. Unlike in our curvatureless method, any restructuring procedure should rely on accurate values of both principal curvatures, to place new nodes on the surface by interpolation.

6. Numerical results

In the numerical results presented below for two deformable drops or bubbles settling under gravity, the characteristic velocity V and time are $|\rho' - \rho_e| g a_2^2 / (8\pi\mu_e)$ and a_2/V, respectively, where a_2 is the largest of the two radii, $a_2 > a_1$, for non-deformed drops. Spherical shapes were taken as the initial condition. Each relative trajectory is uniquely determined by the size ratio a_1/a_2, viscosity ratio λ, initial horizontal $\Delta \tilde{x}_o = \Delta x_o / a_2$ and vertical $\Delta \tilde{z}_o = \Delta z_o / a_2$ offsets of the drop centres, and the Bond number:

$$\mathscr{B} = \frac{|\rho' - \rho_e| g a_2^2}{\sigma} . \tag{6.1}$$

In addition to the features described in §2–5, our algorithm uses Wielandt's deflation for the principal equation (2.1) and biconjugate gradient iterations (Zinchenko *et al.* 1997); the latter are particularly advantageous for small gaps when $\lambda \ll 1$. We have found that neither of the two simple stability criteria, $\Delta t \leqslant K(\Delta x)^{3/2}$ (Rallison &
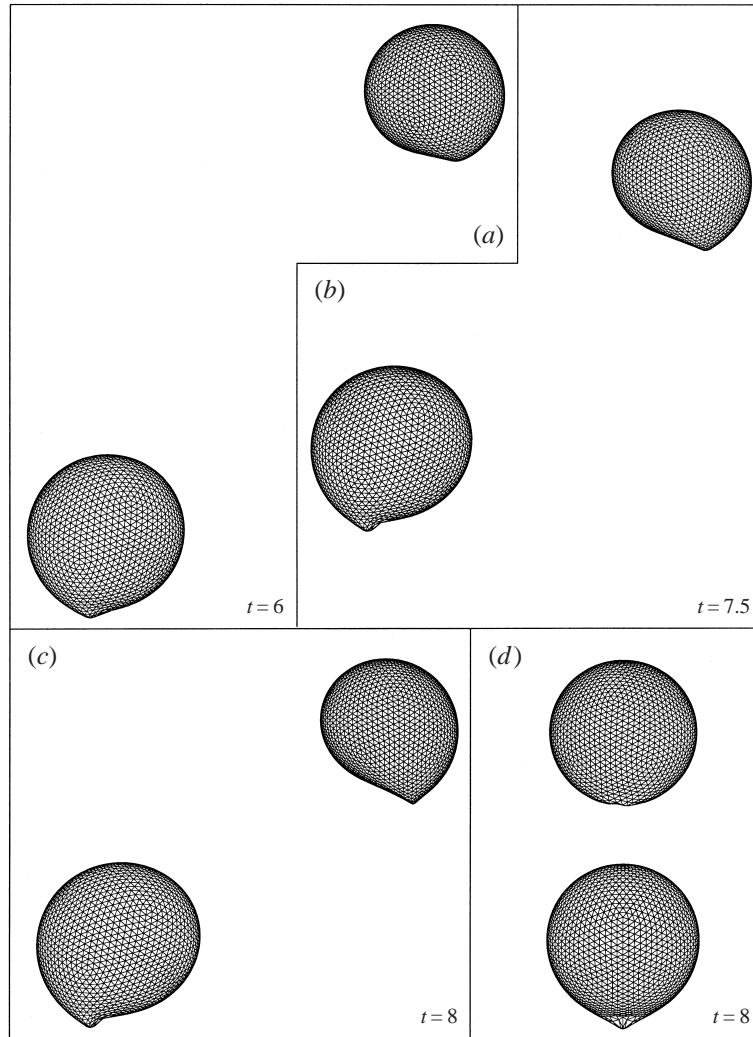
FIGURE 5. Relative buoyancy-driven motion of two bubbles with $a_1/a_2 = 0.9$, $\lambda = 10^{-3}$, $\mathscr{B} = 14.26$, $\Delta\tilde{x}_o = 4.75$, $\Delta\tilde{y}_o = 0$, and $\Delta\tilde{z}_o = 15$ by the curvatureless algorithm with 3840 triangular elements on each surface; no smoothing is used: $(a$–$c)$ the bubble shapes in the (x, z)-plane; (d) in the (y, z)-plane. The calculation could not be continued due to the two-dimensional cusp formation on the upper bubble at $t \approx 8$, without smoothing.

Acrivos 1978) or $\Delta t \leqslant K\Delta x$ (Rallison 1981), where Δx is the minimum mesh edge and $K = $ const, provides the optimum time step in applications with cusped or highly stretched drops, at least for the present mesh adaptation method (§ 5). Instead, a more complicated empirical rule was used (see Appendix C).

6.1. *Capture efficiency of bubbles and low-viscosity drops*

Figure 5 presents an example of relative motion for two bubbles, with $a_1/a_2 = 0.9$, $\lambda = 10^{-3}$, $\mathscr{B} = 14.26$, initial centre-to-centre offsets $\Delta\tilde{x}_o = 4.75$, $\Delta\tilde{y}_o = 0$ and $\Delta\tilde{z}_o = 15$, using the curvatureless algorithm with $N_\Delta = 3840$ triangular elements on each bubble and without smoothing. The formation of apparent singularities on both bubbles can be seen from figure 5(a–c) (front view, in the (x, z)-plane). Most interestingly, the
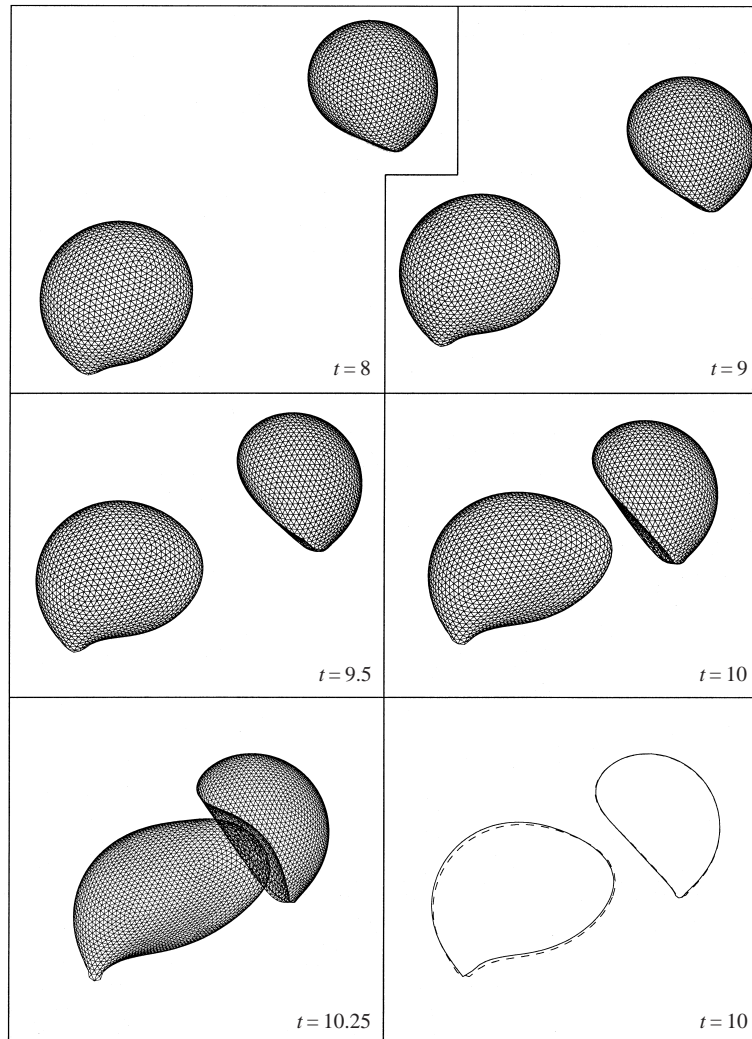
FIGURE 6. The same simulation as in figure 5 in the (x, z)-plane, repeated with smoothing parameters $\epsilon_1 = \epsilon_2 = 6.67 \times 10^{-3}$ and leading to bubble capture. The contour comparison at $t = 10$ is for this simulation with $N_\Delta = 3840$ and $\epsilon_1 = \epsilon_2 = 6.67 \times 10^{-3}$ (dashed lines) and another simulation with $N_\Delta = 6000$ and $\epsilon_1 = \epsilon_2 = 2.14 \times 10^{-3}$ (solid lines).

side view in the (y, z)-plane (figure 5*d*) reveals that the larger, bottom bubble tends to develop a point singularity, while the singularity formed on the smaller bubble by $t = 8$ is scallop-like, which is locally a two-dimensional cusp. The occurrence of such sharp edges can be also seen in related experiments by Manga & Stone (1993, 1995*b*), as shown in figure 1. It is this two-dimensional cusp generating a concentrated capillary force that does not allow the calculation to continue much farther, if the traditional boundary integral (2.4) is used. In contrast, using the curvatureless form (§2) and a small dynamical smoothing (§3) with $\epsilon_1 = \epsilon_2 = \epsilon = 6.67 \times 10^{-3}$, we have been able to repeat the simulation in figure 5 and predict the further motion, resulting in bubble capture (figure 6). This interesting phenomenon of deformation-induced bubble capture was discovered by Manga & Stone (1993, 1995*b*), as shown in figure 1,
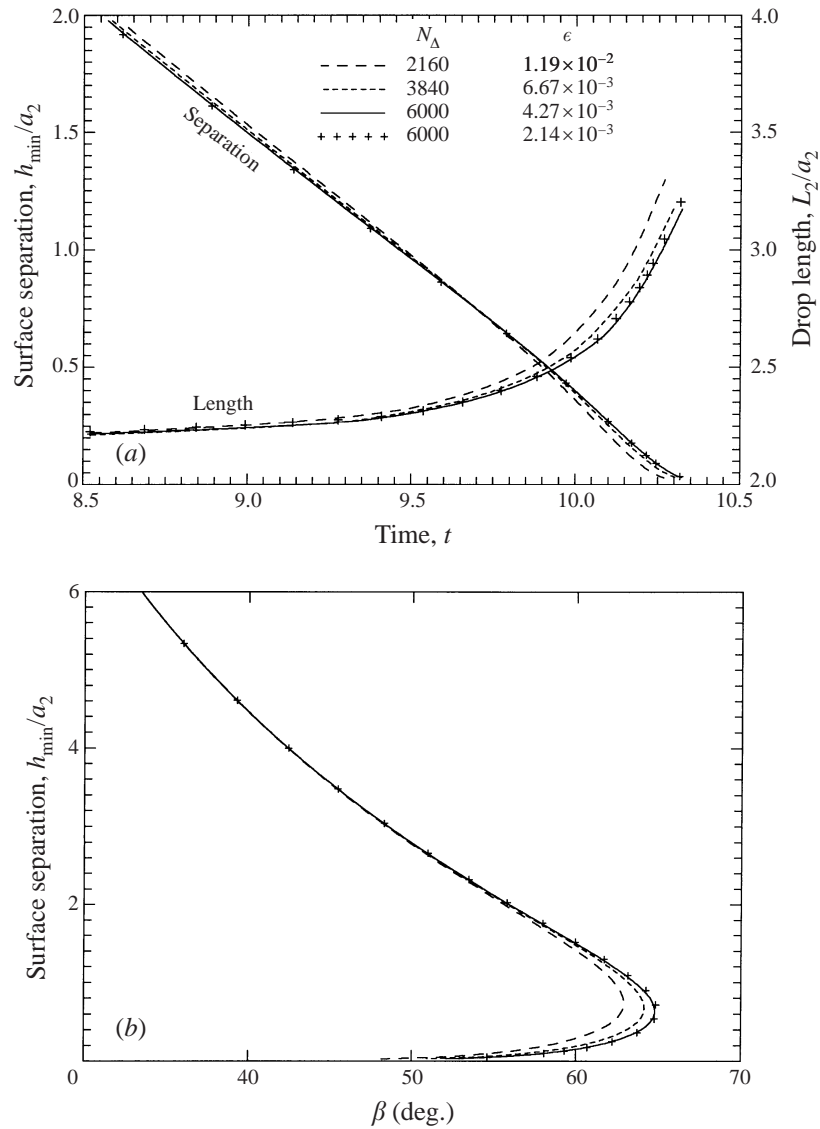
FIGURE 7. The non-dimensional surface clearance, h_{min}/a_2, vs. time (a) and vs. the angle β between the line of surface centroids and the vertical (b) by the curvatureless algorithm. The physical parameters a_1/a_2, λ, $\mathscr{B}$, $\Delta \tilde{x}_o$, and $\Delta \tilde{z}_o$ are the same as in figures 5 and 6; different triangulations and smoothing parameters are used. Also shown in (a) is the non-dimensional length, L_2/a_2, of the larger bubble.

but we are not aware of any adequate three-dimensional simulations close to their experimental range; it is likely that cusping prevented progress with conventional algorithms.

As a check of numerical convergence and correctness of the curvatureless algorithm, we repeated the simulation in figure 6, using $N_\Delta = 2160$, $\epsilon = 1.19 \times 10^{-2}$, and $N_\Delta = 6000$, $\epsilon = 4.27 \times 10^{-3}$, so that the product ϵN_Δ remained at 25.6 for all three runs. The calculation was reasonably fast for $N_\Delta = 2160$ (the whole run from $t = 0$ to 10.25 taking about 2.5 h on an Alpha DEC 5/333 workstation), but required about
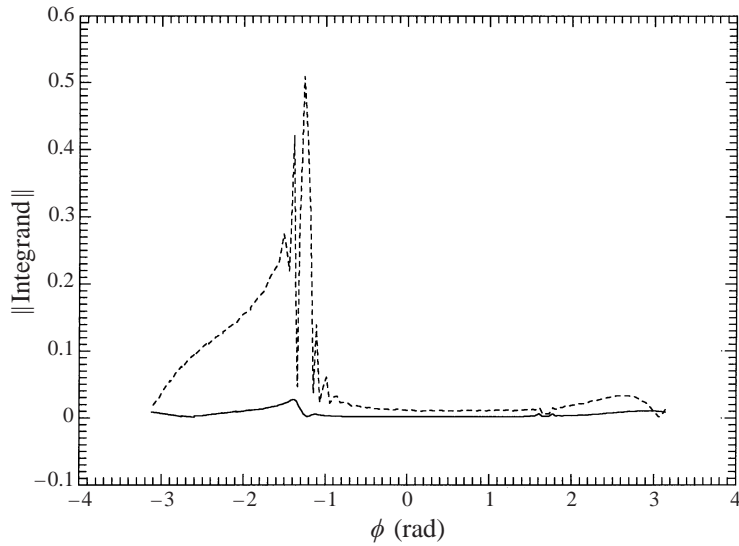
FIGURE 8. Comparison of the integrands in the $x_2 = 0$ plane on the smaller bubble at $t = 9$ vs. angle ϕ of rotation around the bubble centre. The parameters a_1/a_2, λ, $\mathscr{B}$, $\Delta\tilde{x}_o$, $\Delta\tilde{z}_o$, N_Δ, and ϵ are the same as in the first five frames of figure 6. The dashed line is for the regularized conventional integral form (2.5), the solid line is for the curvatureless integrand (2.11). A much larger contribution of the two-dimensional cusp region to the conventional integral (2.5) is seen.

two days for $N_\Delta = 6000$, not only due to the $O(N_\Delta^2)$ boundary-integral scaling, but also due to sharper singularities and the reduced time step (see (C1)). Figure 7(a) presents the non-dimensional minimum surface separation h_{min}/a_2 (calculated as described in Zinchenko *et al.* 1997) and length of the larger drop versus time, while figure 7(b) gives h_{min}/a_2 vs. the angle β between the line of bubble centres and the vertical (the centres being defined as surface centroids). The behaviour in figure 7(b) is typical for coating of the smaller bubble on the front of the larger one, when β first increases as time proceeds, reaches a maximum, and then decreases, suggesting stability of the vertically aligned configuration (Manga & Stone 1993, 1995b). In practice, coalescence eventually occurs due to van der Waals attraction, but the actual coalescence time depends on the details of near-contact physics. Figures 7(a) and 7(b) demonstrate the global numerical convergence for $N_\Delta \to \infty$ and $\epsilon \to 0$ with the present method of treating singularities. The errors decrease approximately in proportion to $1/N_\Delta$, although the rate of convergence is modest in the final stages of the simulation due to cusping.

We have also checked that the global convergence at $N_\Delta \to \infty$ and $\epsilon \to 0$ is independent of the relation between $\epsilon \ll 1$ and $N_\Delta \gg 1$, by repeating the calculation with $N_\Delta = 6000$ using a different value $\epsilon = 2.14 \times 10^{-3}$ of the smoothing parameter (crosses in figure 7a, b). The results are nearly indistinguishable from those with $N_\Delta = 6000$ and $\epsilon = 4.27 \times 10^{-3}$. Finally, the comparison of the absolute positions and shapes of the bubbles at $t = 10$ for two two runs ($N_\Delta = 3840$, $\epsilon = 6.67 \times 10^{-3}$, and $N_\Delta = 6000$, $\epsilon = 2.14 \times 10^{-3}$) in the last frame of figure 6 confirms the global numerical convergence.

It is useful to see in detail how the curvatureless form eliminates the contribution of the two-dimensional cusp. We have performed a run with the same triangulation and smoothing as in the first five frames of figure 6, but using the conventional

integral form (2.5) with the standard singularity and near-singularity subtraction, and compared the regularized integrand for (2.5) with the curvatureless integrand (2.11) on the smaller bubble at $t = 9$. In this comparison, the observation point y was fixed at the top of the smaller bubble, with the integration point x running in the plane of the drawing ($x_2 \approx 0$) only. In figure 8, the modulus (norm) of the non-dimensional integrand is shown vs. the angle ϕ of rotation of $x - x_1$ around the drop centroid x_1, both for the curvatureless (solid line) and conventional (dashed line) calculations. Both regularized integrands are finite, although discontinuous, at $x = y$ ($\phi \approx 1.67$), but the cusp contribution to the conventional integral (2.5) is much larger. It is this $O(1)$ contribution which breaks down the conventional calculation at $t \approx 9.36$, despite smoothing, when the mesh fails to resolve the strengthening cusp. The surface separation at $t = 9.36$ is $1.1a_2$, which is still too large to determine the outcome of the interaction (see figure 7a, b). In contrast, the curvatureless form is not crucially dependent on cusp resolution and proceeds to much smaller separations.

As an additional illustration and check of the correctness of the new, curvatureless algorithm, we analysed the case $a_1/a_2 = 0.7$, $\lambda = 10^{-3}$, $\mathscr{B} = 7$, $\Delta \tilde{x}_o = 2.3$, and $\Delta \tilde{z}_o = 10$. In this case, the smaller bubble is swept around the larger one and develops a point singularity (figure 9). Without smoothing, the calculation could not proceed beyond $t = 3.8$–3.9 and so the ultimate outcome of the interaction could not be determined. However, using a small smoothing parameter $\epsilon_1 = 3.3 \times 10^{-3}$ ($\epsilon_2 = 0$) and $N_\Delta = 3840$ triangular elements per bubble, we are able to predict that the smaller bubble eventually becomes sucked into the dimple formed at the rear of the larger one, even though the sharp tip is not finely resolved (figure 9). This mode of bubble capture is shown in figure 1 and is referred to as entrainment (Manga & Stone 1993, 1995b). Unlike in figure 5, no line singularity develops in this case, and so a conventional boundary-integral formulation (2.4) with smoothing is also successful. A comparison of the minimum separations between the two formulations is given in figure 10 for several triangulations with smoothing, demonstrating that the two methods converge to the same limit as $N_\Delta \to \infty$, $\epsilon \to 0$. At the same triangulation, the curvatureless method gives slightly more accurate $h_{\min}(\beta)$, even at the smallest separations considered. Most importantly, the curvatureless form is the only option when line singularities develop.

In the calculations with smoothed singularities, we used *non-adaptive* meshes prepared by the passive mesh stabilization method of Zinchenko *et al.* (1997) without modifications, except that slight adaptivity was used to demonstrate the development of a line singularity in the run of figure 5 without smoothing. It would seem natural, at least for aesthetical reasons, to use curvature-adaptive meshes in boundary-integral calculations with cusps, but we have so far found this idea to offer no prospect. In part, this finding is because the cusp singularities before smoothing are well beyond the resolution of global numerical methods. We have also found that using an adaptive mesh after smoothing makes the global numerical convergence extremely poor, so that the results of interest can be qualitatively wrong for insufficient triangulations. For example, in runs with $a_1/a_2 = 0.9$, $\lambda = 10^{-3}$, $\mathscr{B} = 14.26$, $\Delta \tilde{x}_o = 4.75$, and $\Delta \tilde{z}_o = 15$, we had no capture (in contrast to that shown in figure 6), and the results for adaptive meshes only started to converge to the correct behaviour when several thousand elements per bubble were used. This poor convergence likely happens because adaptivity makes the mesh too non-uniform in the transition region from the cusp to the smooth part, with a negative effect on the global accuracy. Most recently, we have also experimented with some alternative, differential forms of the smoothing mechanism, and found that they can provide a better convergence for $h_{\min}$ than in figure 7(b); however,
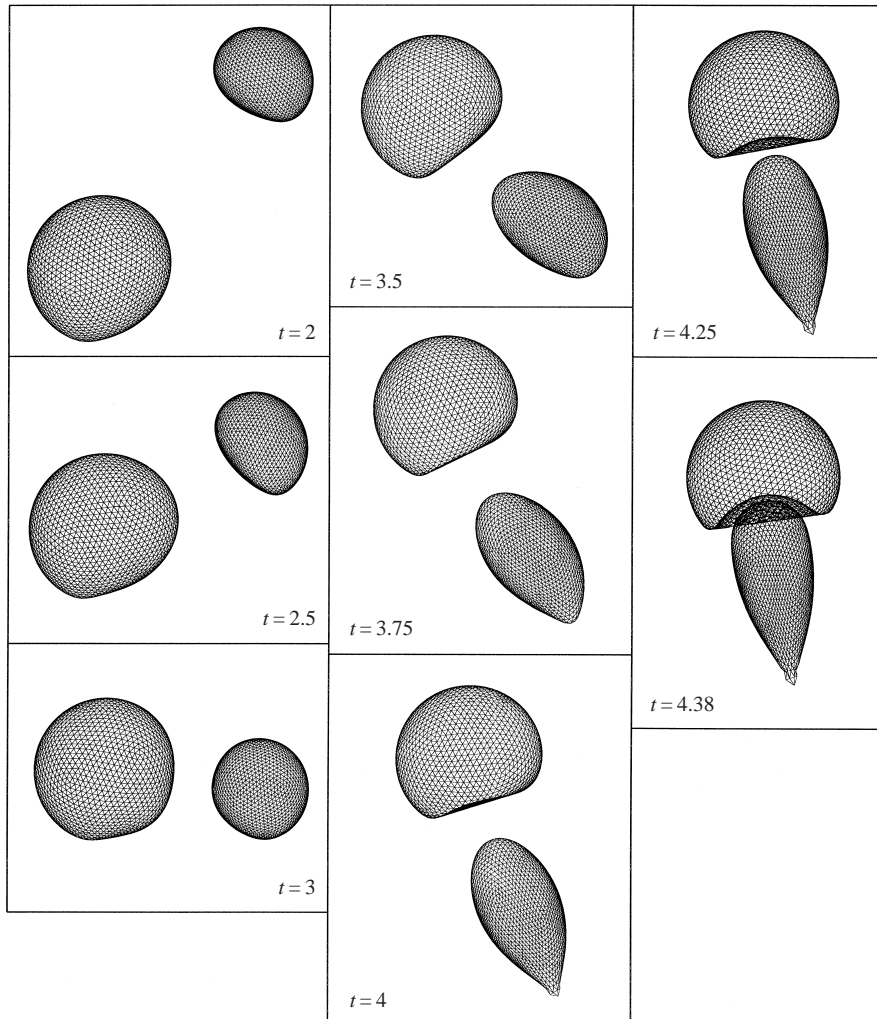
FIGURE 9. Relative buoyancy-driven motion of two bubbles with $a_1/a_2 = 0.7$, $\lambda = 10^{-3}$, $\mathscr{B} = 7$, $\Delta\tilde{x}_o = 2.3$, and $\Delta\tilde{z}_o = 10$ by the curvatureless algorithm with $N_\Delta = 3840$ triangular elements on each surface and the smoothing parameter $\epsilon_1 = 3.3 \times 10^{-3}$ for the smaller bubble.

these forms led to a poorer convergence for the overall shapes, and they were not used in our systematic calculations of the capture efficiency (see below). Although a better form of the smoothing mechanism may still be found, it may not necessarily be one of strong physical motivation; an analogy with artificial viscosity in computational hydrodynamics can be recalled (see, for example, Richtmyer & Morton 1967).

The present method has allowed us to calculate, for the first time, the capture efficiency $E = [(\Delta x_o)_{\mathrm{cr}}/(a_1 + a_2)]^2$ of bubbles and low-viscosity drops at moderate and moderately large Bond numbers. Boundary-integral simulations were performed with an initial dimensionless vertical offset of $\Delta\tilde{z}_o = 10$–20 and a dimensionless initial horizontal offset, $\Delta\tilde{x}_o$, which was varied by trial and error until entrainment and separation trajectories were found for which the two respective $\Delta\tilde{x}_o$ values differ by no more than 0.05–0.1. Small corrections (always less than 5%) to the critical horizontal offsets $(\Delta\tilde{x}_o)_{\mathrm{cr}}$, below which capture occurs, were then made to effectively
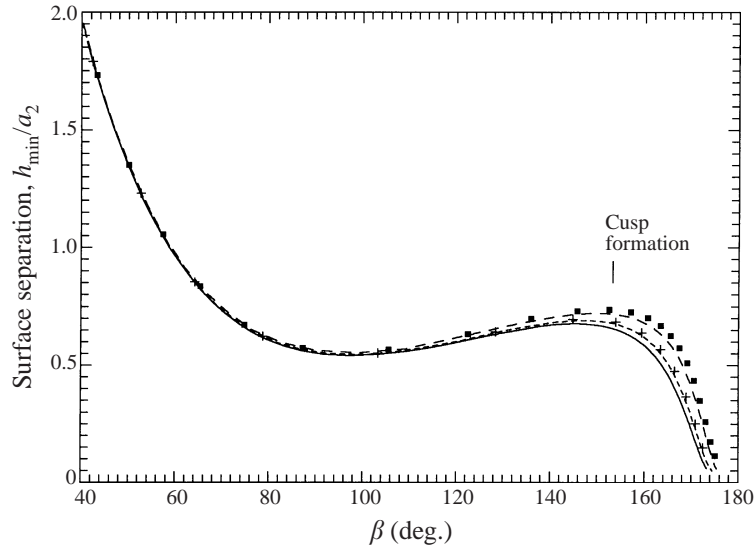
FIGURE 10. The non-dimensional surface clearance, $h_{\min}/a_2$, vs. the angle β between the line of surface centroids and the vertical. The physical parameters a_1/a_2, λ, $\mathscr{B}$, $\Delta\tilde{x}_o$, and $\Delta\tilde{z}_o$ are the same as in figure 9. The long-dashed line (curvatureless formulation) and dark squares (conventional formulation) are for $N_\Delta = 1280$, $\epsilon_1 = 0.01$. The short-dashed line (curvatureless formulation) and crosses (conventional formulation) are for $N_\Delta = 2160$, $\epsilon_1 = 5.93 \times 10^{-3}$. The solid line is for the curvatureless formulation with $N_\Delta = 3840$ and $\epsilon_1 = 3.33 \times 10^{-3}$.

infinite initial vertical offsets by performing additional boundary-integral simulations with $\Delta\tilde{z}_o = 50$. For comparison, the far-field motion was also determined using the analytical results of Manga & Stone (1993), which includes both an outward drift due to far-field hydrodynamic interactions of spherical drops and an inward drift due to small deformations. We found that the deformation-induced inward drift predicted by the quasi-steady small-deformation theory is generally greater than that given by the boundary-integral simulations, especially at large Bond numbers. Most simulations to find the capture efficiency were performed with 720 or 1280 triangles per bubble or drop, although a few were repeated with greater resolution to check for convergence. The drops and bubbles were started with spherical shapes in most runs. Repeats with ellipsoidal initial shapes, as determined from the small-deformation theory of Manga & Stone (1993) gave no significant differences in the critical horizontal offset for capture.

Results for $E^{1/2} = (\Delta x_o)_{\mathrm{cr}}/(a_1 + a_2)$ versus Bond number are presented in figure 11 for different size ratios a_1/a_2 and viscosity ratios of $\lambda = 10^{-3}$ and $\lambda = 0.1$ (at $a_1/a_2 = 0.7$ only). The critical offset or capture efficiency increases with $\mathscr{B}$ due to increased deformation-induced alignment but becomes only a weak function of $\mathscr{B}$ for large Bond numbers. Also, the critical offset is very sensitive to the size ratio a_1/a_2. As the smaller bubble or drop becomes closer in size to the larger one, both drops experience more deformation and inward drift (Manga & Stone 1993), and they separate more slowly, so that the capture efficiency becomes large. The curves in figure 11 do not exclude the existence of finite critical values $\mathscr{B}_{\mathrm{cr}}(a_1/a_2, \lambda)$ with $E = 0$, as might be anticipated from the axisymmetric calculations of Davis (1999) showing that a finite Bond number is required for entrainment of the smaller drop or bubble in the dimple on the rear of the larger one. It would be very difficult, however, to
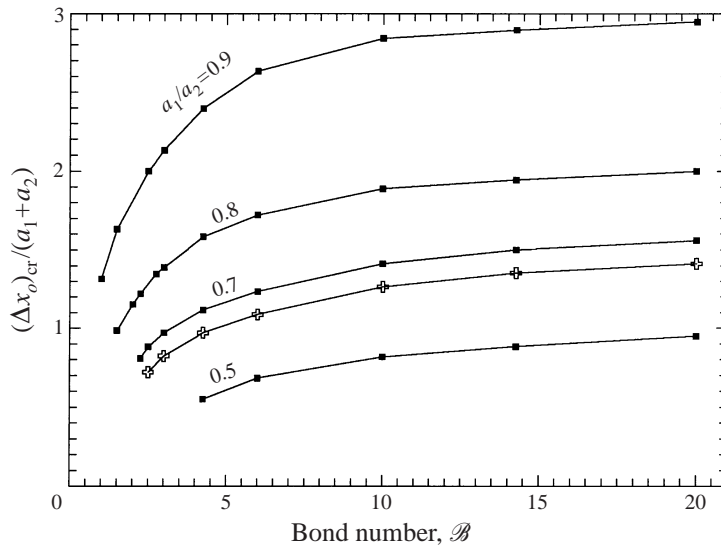
FIGURE 11. The non-dimensional critical capture offset, $(\Delta x_o)_{\mathrm{cr}}/(a_1 + a_2)$, far upstream as a function of the Bond number for bubbles and low-viscosity drops. Dark squares are for $\lambda = 10^{-3}$, crosses are for $\lambda = 0.1$ (at $a_1/a_2 = 0.7$ only).

make three-dimensional calculations to determine these critical values of the Bond number for $\lambda \ll 1$, because long-time relative motion of bubbles/drops in very close contact would have to be considered. For $\mathscr{B} \ll 1$, this deformation-induced capture mechanism is absent, and small deformations in the region of close contact retard the film drainage, so that molecular attractions (such as van der Waals forces) are required for non-zero capture efficiencies (Rother, Zinchenko & Davis 1997). It is of interest to note that $\mathscr{B} = 0$ is a singular limit, since perfectly spherical drops and bubbles have finite values of E in the absence of molecular attractions (Zinchenko 1982; Zhang & Davis 1991). Finally, a comparison of the dark squares and the crosses in figure 11 at $a_1/a_2 = 0.7$ shows that the capture efficiency is slightly reduced when the bubbles ($\lambda = 10^{-3}$, which is representative of $\lambda \leqslant O(10^{-2})$) are replaced with drops having $\lambda = 0.1$. With the increased viscosity of the internal phase, both the rate and quasi-steady amount of deformation are reduced (Manga & Stone 1993). For $\lambda = O(1)$, the capture phenomenon is complicated by drop breakup, as discussed in the next two subsections.

The predicted values of the critical capture offsets are compared in figure 12 with experimental measurements by Manga & Stone (1995b). The experiments used air bubbles in a viscous corn syrup, with four fixed sizes of the larger bubble such that $\mathscr{B} = 15, 30, 73,$ and 120. The initial horizontal offset was varied, resulting in either capture (filled symbols) or separation (open symbols). The solid line in figure 12 is the prediction from the current work for $\mathscr{B} = 15$. We have not attempted calculations for $\mathscr{B} > 20$, anticipating poor numerical convergence, since the bubble shapes with cusping are no longer compact for high Bond numbers. However, figure 11 indicates that the critical capture offset increases only weakly with large Bond numbers. On average, the critical offsets inferred from the experiments fall slightly below the predicted ones (perhaps due to finite-container effects), but the data support the main predicted trends of the capture efficiency increasing strongly with size ratio and only weakly with Bond number. The dashed lines in figure 12 are from the empirical
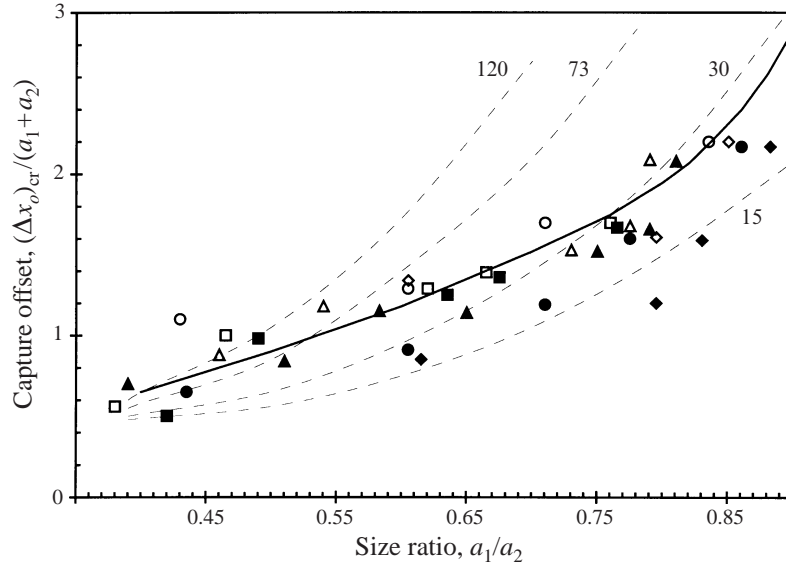
FIGURE 12. Comparison of predicted critical capture offset for bubbles from present work (solid line, for $\mathscr{B} = 15$) with the experiments in figures 13 and 14 of Manga & Stone (1995*b*) for $\mathscr{B} = 15$ (diamonds), 30 (circles), 73 (triangles), and 120 (squares). The open symbols are for experiment trajectories which resulted in separation, whereas the closed symbols are for entrainment. The solid line is the predicted division of the open symbols above from the closed symbols below. The dashed lines are from the empirical correlation (6.2), with $\mathscr{B} = 15$, 30, 73, and 120 (bottom to top).

correlation of Manga & Stone (1995*b*):

$$\frac{(\Delta x_o)^2_{\text{cr}}}{(a_1 + a_2)^2} = 0.3 \left(\frac{a_1}{a_2}\right)^{1/2} + \tfrac{1}{2}\,\mathscr{B}\left(\frac{a_1}{a_2}\right)^6, \qquad (6.2)$$

where the first term on the right-hand side is an approximate fit of the capture efficiencies of Zhang & Davis (1991) for spherical drops ($\mathscr{B} = 0$) and the second term is motivated by the deformation-induced entrainment mechanism of interest here. This correlation has similar trends to those predicted in the current work, except that the square-root dependence of the critical offset on Bond number when the second term on the right-hand side of (6.2) dominates is stronger than that seen in figure 11 for large $\mathscr{B}$. The experimental data (which in figure 12 include results for $\mathscr{B} = 73$ and 120 which Manga & Stone (1995*b*) did not use in developing (6.2), due to large predicted far-field deformations) are perhaps too sparse to make a firm judgment, but they appear to support only a weak dependence of the critical capture offset on $\mathscr{B}$ in the range studied.

6.2. *Breakup simulations*

Interestingly, capture by coating or entrainment, observed by Manga & Stone (1993, 1995*b*) and analysed in §6.1 of the present paper, is only one of several possible outcomes for two deformable drops settling under gravity. For $\lambda = O(1)$, it has been shown (Zinchenko *et al.* 1997; Cristini *et al.* 1998) that, instead of capture, breakup of the smaller drop may typically occur. In particular, figures 17 and 18 of Zinchenko *et al.* (1997) for $a_1/a_2 = 0.7$, $\lambda = 1$, $\mathscr{B} = 5.3125$, $\Delta \tilde{x}_o = 1$, and $\Delta \tilde{z}_o = 5.087$ show that the smaller drop is predicted to break, but the algorithm failed at the very beginning of the neck formation ($t \approx 6$). We have repeated this simulation, using the new,
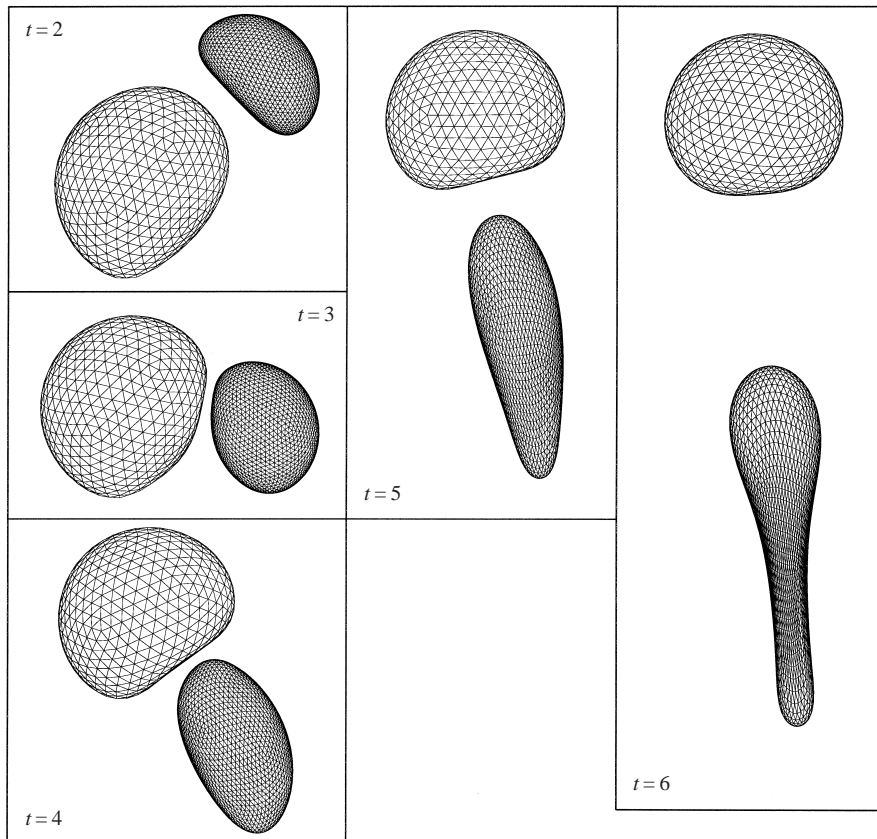
FIGURE 13. Relative buoyancy-driven motion of two drops with $a_1/a_2 = 0.7$, $\lambda = 1$, $\mathscr{B} = 5.3125$, $\Delta \tilde{x}_o = 1$, and $\Delta \tilde{z}_o = 5.087$ by the curvatureless algorithm with 3840 triangular elements on the smaller drop and 1280 elements on the larger drop.

curvatureless algorithm with the adaptive passive mesh stabilization (§5) based on (5.3). We used $N_{\Delta_2} = 1280$ triangular elements on the larger drop and four different triangulations $N_{\Delta_1} = 2160$, 3840, 6000, and 8640 on the smaller drop. The parameter γ in (4.5) for these and the following simulations was 0.5. The beginning of the process is shown in figure 13 for $N_{\Delta_1} = 3840$. The smaller drop is swept around the larger one, stretches due to hydrodynamical interaction and starts necking. Figure 13 also shows that the new passive mesh stabilization (§5) maintains a high-quality mesh of stretched but open triangles adapted to the high curvature at the tip, while the previous, non-adaptive mesh stabilization method did not prevent the triangles from degeneration, even at $t = 5$ and 5.5 (note the darkened areas in the middle of the drop in figure 17 of Zinchenko *et al.* 1997). The new code allows the calculations to proceed much farther. After $t = 6$, the drops continue to separate, while the smaller one stretches and experiences neck pinchoff. In figure 14, for the simulation with $N_{\Delta_1} = 6000$, only the breaking drop is shown. The other drop remains compact. As time proceeds, the tip of the breaking drop becomes more bulbous. Some depletion of collocation nodes in the bulbous lower part is due to their slow migration to the neck region (as explained in §5), to increase the stability of the calculation and maintain the total number of collocation nodes fixed. The mesh triangles are highly stretched in the middle of the drop, but somewhat more compact in the transition
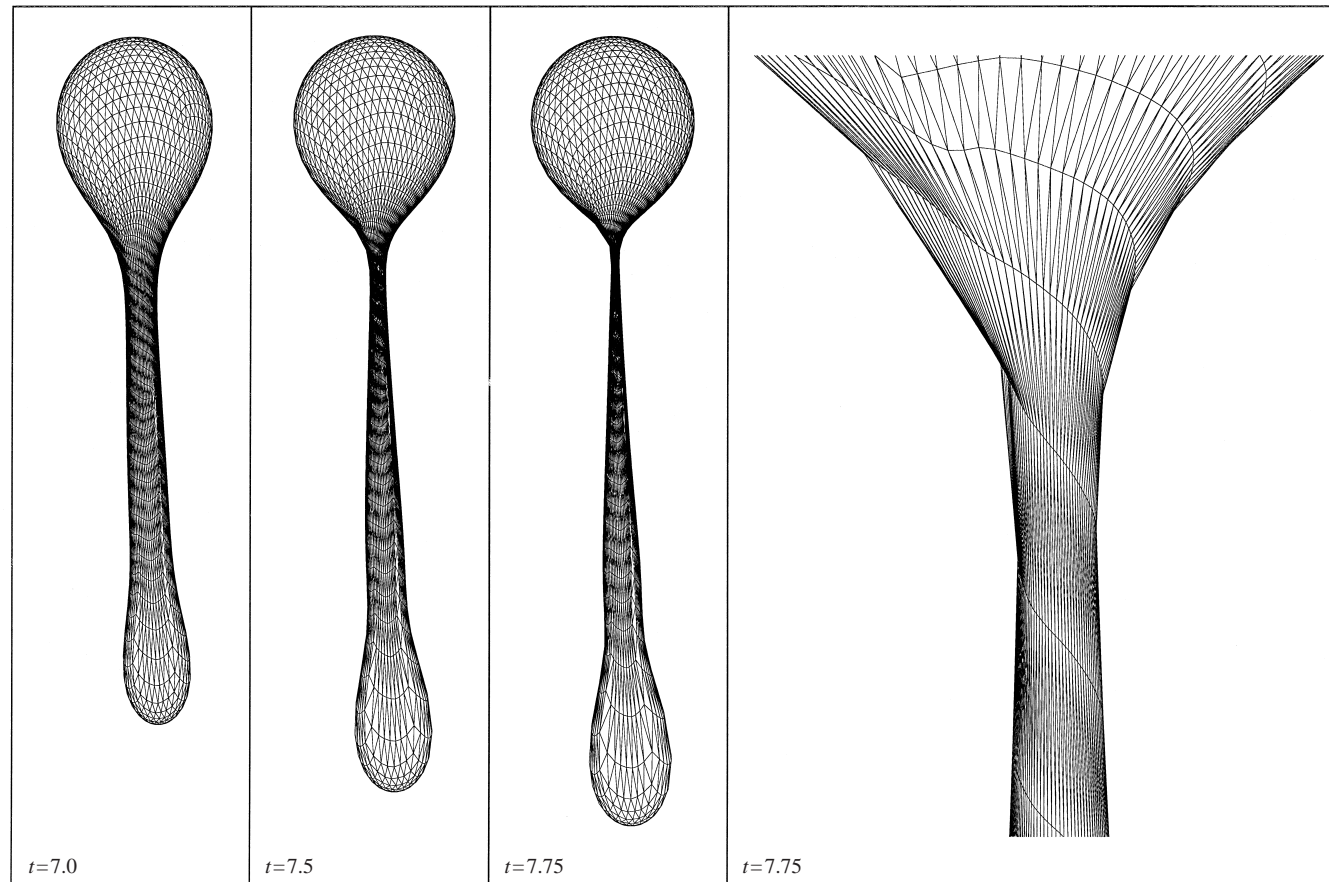
t=7.0   t=7.5   t=7.75   t=7.75

FIGURE 14. The stretching and breakup of the smaller drop (the larger one remains compact). The parameters are the same as in figure 13, except that 6000 triangular elements are used for the smaller drop. The closeup of the neck region in the final frame is magnified 9.54 times from the previous frame.
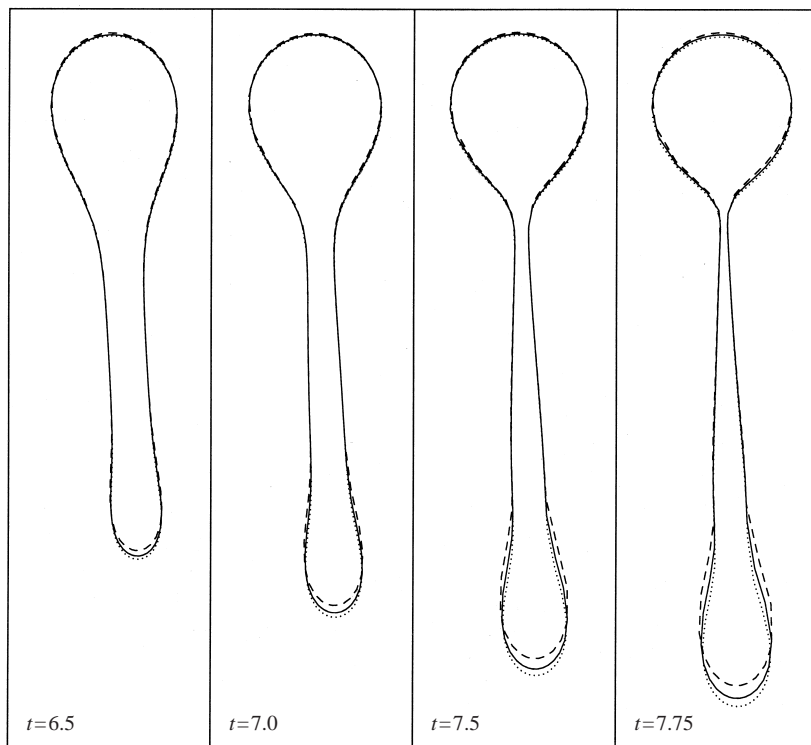
FIGURE 15. Comparison of the absolute positions and shapes of the smaller drop in the (x, z)-plane at different times for the simulation of figure 14 using $N_{\Delta_2} = 3840$ (dashed lines), 6000 (solid lines), and 8640 (dotted lines).

region, as revealed in figure 14 by the close-up at $t = 7.75$. Contour comparisons in the (x, z)-plane for $t = 6.5$–7.75 between the runs with $N_{\Delta_1} = 3840$, 6000, and 8640 are shown in figure 15. Convergence is excellent in the top and middle parts of the smaller drop, but deteriorates somewhat at the bottom near the end of the simulation. Namely, the less accurate solution with $N_{\Delta_1} = 3840$ slightly overestimates the size of the bottom bulb, but underestimates the overall drop length.

The drop breakup time is finite and can be found with good accuracy by extrapolation. To this end, the drop surface was approximated as a polyhedron with flat faces, and the minimum area $S_{\min}$ of polygonal cross-sections orthogonal to the line of maximum elongation was used to find an equivalent neck radius $r = (S_{\min}/\pi)^{1/2}$. The use of an equivalent radius is justified by the observation that the local neck shape in our three-dimensional calculations becomes axisymmetrical, as breakup is approached. This supports, incidentally, the body of local axisymmetrical studies on viscous pinchoff (see, for example, Eggers 1993, 1997; Papageorgiou 1995; Brenner, Lister & Stone 1996; and Lister & Stone 1998). In particular, the neck radius was predicted to decrease linearly in time at pinchoff both for a free-surface thread (Papageorgiou 1995) and for a thread surrounded by another fluid (Lister & Stone 1998). It is of particular interest to see if our global three-dimensional solution is in agreement with these predictions. In figure 16, r/a_1 is shown as a function of time for all the simulations with $\lambda = 1$ described above. Surprisingly, this dependence becomes linear at t as small as 6.8, when the neck is still quite thick. An extrapolation to zero neck radius using the best linear fits in the range $7 < t < 7.75$ gives very close breakup
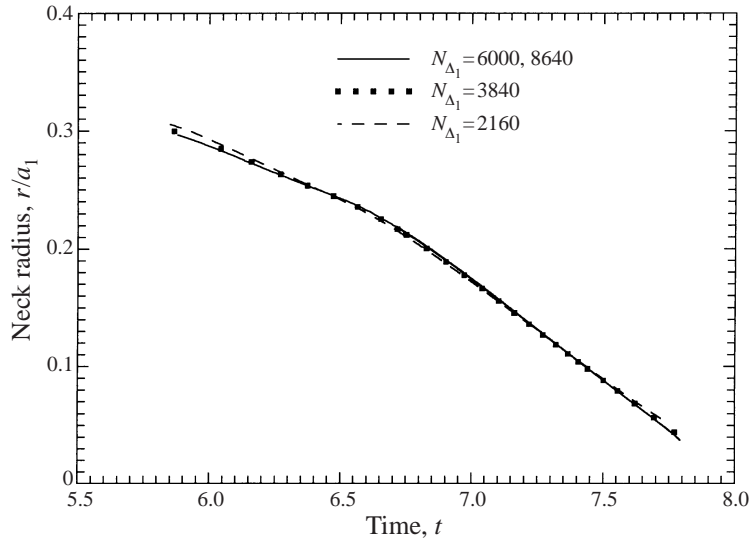
FIGURE 16. The non-dimensional equivalent neck radius, r/a_1, vs. time for the simulation of figure 14 using $N_{\Delta_2} = 1280$ and several values of N_{Δ_1}. The results for $N_{\Delta_1} = 8640$ and 6000 are practically indistinguishable.

times of $t_{cr} = 8.05$ ($N_{\Delta_1} = 2160$), 8.03 ($N_{\Delta_1} = 3840$) and 8.02 ($N_{\Delta_1} = 6000$ and 8640) for all three triangulations. The small lack of accuracy at the bottom of the drop at large times (see figure 15) does not seem to appreciably affect the dynamics of the neck thinning; this may be due to universality of self-similar thinning at pinchoff. However, the dimensional slope of the neck radius versus time from the apparently linear range $7 < t < 7.75$ in figure 16 is $-0.025 \, \sigma/\mu$, which is slightly smaller in magnitude than the value of $-0.034 \, \sigma/\mu$ predicted for very small necks at $\lambda = 1$ by the self-similar axisymmetrical solution of Lister & Stone (1998). We have continued our simulations with $N_{\Delta_1} = 6000$ and 8640 to $t = 7.79$ to verify that the thinning accelerates at the latest stage of breakup. The neck radii for $N_{\Delta_1} = 6000$ and 8640 remain practically indistinguishable, and our average dimensional slope in the range $7.75 < t < 7.79$ is $-0.029 \, \sigma/\mu$, which is closer to the result of Lister & Stone (1998). A similar behaviour of $r(t)$, when the ultimate value of dr/dt is approached only for very thin necks, was seen previously in axisymmetrical simulations of Lister & Stone (1998) and Davis (1999). Knowledge of the final thinning rate from the axisymmetric analysis, together with the three-dimensional simulations, allows tight bounds on the breakup time. Assuming that the slope of $r(t)$ in the present example abruptly changes at $t = 7.79$ to its asymptotic value of Lister & Stone (1998) gives the lower estimate of $t_{br} = 7.95$, which is within 1% of the upper estimate of $t_{br} = 8.02$.

Our simulations also allow accurate determination of the volumes of the drop fragments after breakup. In particular, an equivalent radius a_3 of the larger fragment can be found using the volume of the drop polyhedron (see above) lying above the neck cross-section, and then extrapolating it to zero neck thickness. Neglecting the curvature of the triangular elements in this volume calculation introduces a small error, but this is expected to be less than the error due to long-time integration. Figure 17 shows that, as breakup is approached, the size a_3 of the upper part first decreases due to pinching, then stabilizes and very slightly grows near the end of the simulation; the latter increase is probably a marginal numerical effect, since it tends to
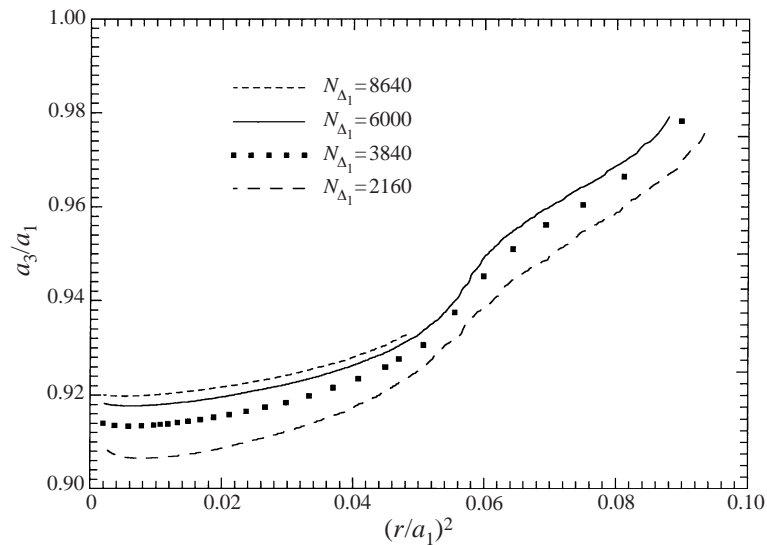
FIGURE 17. The equivalent non-dimensional radius a_3/a_1 of the top fragment vs. non-dimensional neck area $(r/a_1)^2$, as breakup of the smaller drop is approached, for the simulation of figure 14 with $N_{\Delta_2} = 1280$ and several values of N_{Δ_1}.

disappear for fine triangulations. The radius of the main (top) fragment after breakup is $a_3 = 0.907\, a_1$ ($N_{\Delta_1} = 2160$), $a_3 = 0.914\, a_1$ ($N_{\Delta_1} = 3840$), $a_3 = 0.918\, a_1$ ($N_{\Delta_1} = 6000$), and $a_3 = 0.920\, a_1$ ($N_{\Delta_1} = 8640$), with very good convergence at $N_{\Delta_1} \to \infty$.

We did not increase the number $N_{\Delta_2} = 1280$ of triangular elements on the larger drop for the simulations of figures 13–17, expecting this refinement to have a marginal effect. The simulations from $t = 0$ to $t \approx 7.75$ took about 1.7 h, 5 h, 12.5 h, and 27.8 h of CPU time for $N_{\Delta_1} = 2160$, 3840, 6000, and 8640, respectively, on an Alpha DEC 5/333 workstation, with the last stage (after necking) being the most time consuming, due to a smaller time step (see Appendix C). To reach this speed, the scalar curvatureless integral (2.7) for the normal velocity was used for well-separated drops, which is sufficient and much faster for this special case $\lambda = 1$ than using the vector integral (2.11).

The combination of the present mesh stabilization method with the curvatureless formulation was essential in the above simulations. When we switched to the traditional integral form (2.5), it was not possible to proceed beyond $t = 6.25$–6.30, probably because the errors of the curvature calculation on a stretched mesh destroy the solution (see below). Presumably, the traditional integral (2.5) would require a mesh of compact (nearly equilateral) triangles to be successful in breakup simulations. Such a mesh could be obtained by dynamical restructuring, with an increase in the total number of boundary elements as the drop stretches. The present approach offers an alternative way of doing breakup simulations, which takes advantage of the slow spatial variations of unknowns along the length of elongated drops by using a highly stretched mesh with a fixed number of boundary elements and fixed connections.

To proceed to long times in our breakup simulations, it was also crucial to use the mesh stabilization function in the form (5.3), rather than (5.7). As explained in §5, the form (5.7) does not contain a mechanism of (slow) migration of collocation nodes to the neck region; besides, using a triangle area S_Δ in (5.7) instead of the quality function Q_Δ in (5.3) gives improper control over mesh degeneration close to breakup,
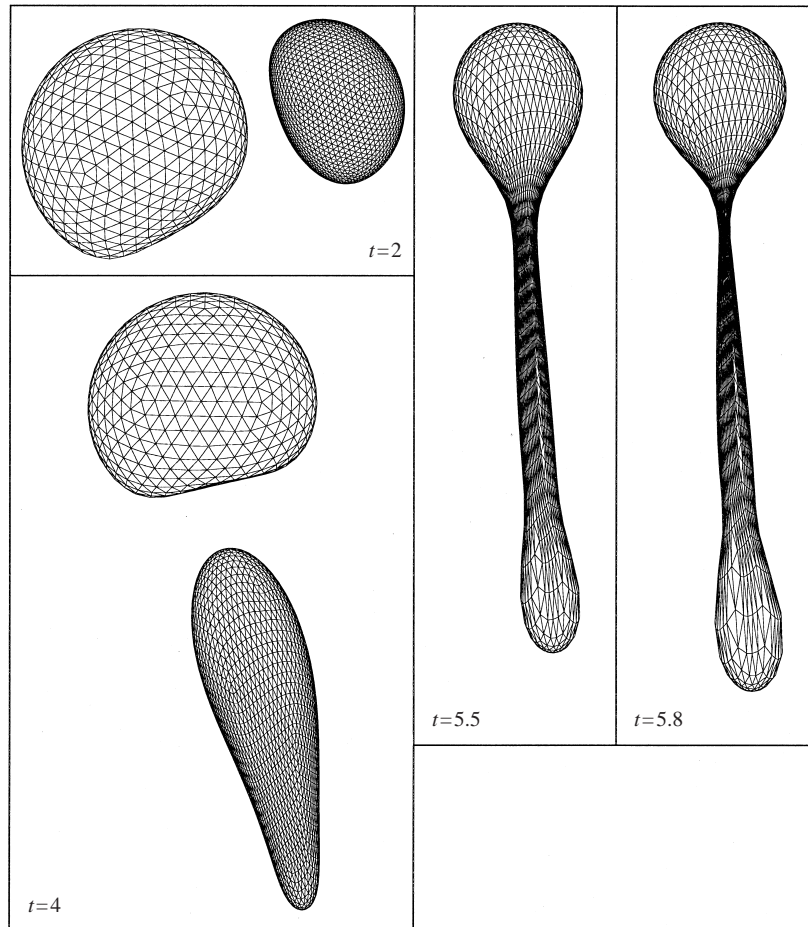
FIGURE 18. Relative buoyancy-driven motion of two drops with $a_1/a_2 = 0.7$, $\lambda = 0.5$, $\mathcal{B} = 6$, $\Delta\tilde{x}_o = 1$, and $\Delta\tilde{z}_o = 5$ by the curvatureless algorithm with 3840 triangular elements on the smaller drop and 1280 elements on the larger drop. Only the smaller breaking drop is shown at $t = 5.5$ and 5.8.

which led to a highly irregular mesh in the neck region and the middle part of the drop for $t > 7.25$ and incorrect dynamics of the neck thinning. Interestingly, however, the solution using (5.7) was not totally destroyed until $t \approx 7.50$, owing to the curvatureless formulation which makes the simulations globally less sensitive to the mesh quality than the traditional form (2.5). On the other hand, for intermediate deformations ($t \leqslant 7$–7.25), the form (5.7) is able to describe drop length more accurately, and so is recommended for all conditions except for drops close to breakup, where (5.3) is the only choice of the two.

In a more difficult case of an essentially supercritical drop breakup at $\lambda \neq 1$, the present code also allows prediction of the volumes of the drop fragments after breakup, with modest triangulations. The simulation in figure 18 is for $\lambda = 0.5$, $a_1/a_2 = 0.7$, $\mathcal{B} = 6$, $\Delta\tilde{x}_o = 1$, $\Delta\tilde{z}_o = 5$, $N_{\Delta_1} = 3840$, and $N_{\Delta_2} = 1280$. Unlike for $\lambda = 1$, the case $\lambda \neq 1$ presents a more noticeable limitation on how close to breakup the code can approach with a given triangulation. For $N_{\Delta_1} = 3840$ shown in figure 18, the run failed after $t = 5.80$ due to divergence of velocity iterations, obviously because the double-layer
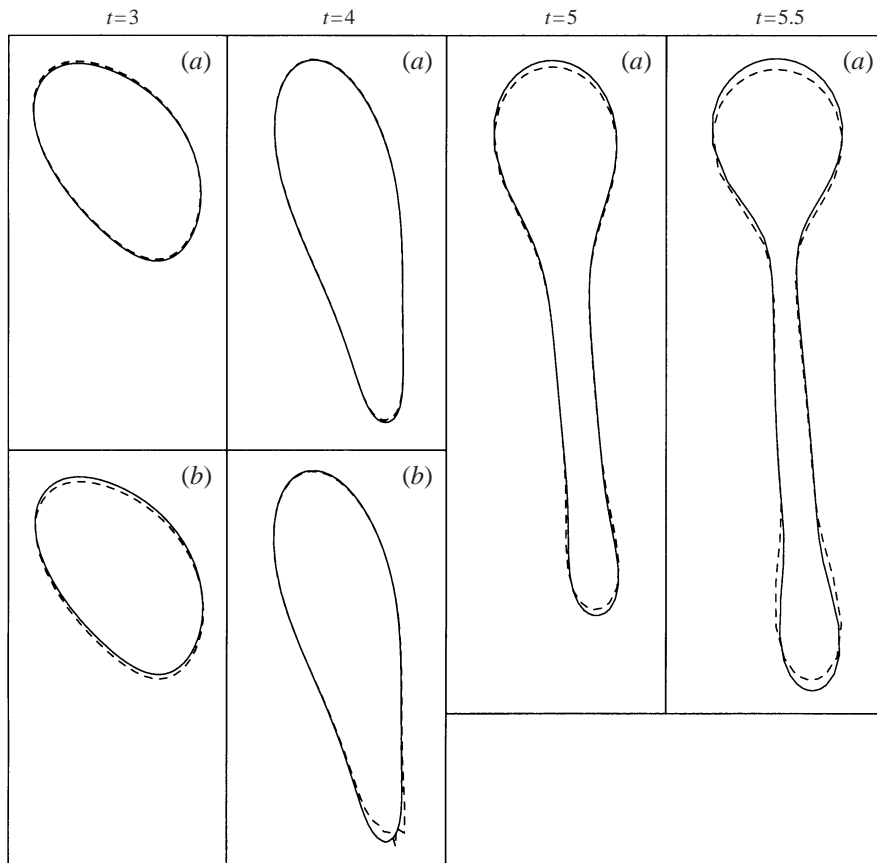
FIGURE 19. Comparison of the absolute positions and shapes of the smaller drop in the (x, z)-plane at different times between the simulation shown in figure 18 and a similar simulation using 2160 triangular elements on the smaller drop and the curvatureless algorithm (a); the solid lines are for $N_{\Delta_1} = 3840$ and the dashed lines are for $N_{\Delta_1} = 2160$. (b) A similar comparison, using the conventional boundary-integral formulation both for $N_{\Delta_1} = 3840$ (solid lines) and $N_{\Delta_1} = 2160$ (dashed lines).

discretization was poor in the neck region. To test the convergence, a similar run was made using the present code with $N_{\Delta_1} = 2160$ and $N_{\Delta_2} = 1280$. This run took only 3.5 h on an Alpha DEC 5/333 workstation (vs. 10 h for $N_{\Delta_1} = 3840$ and $N_{\Delta_2} = 1280$) to reach $t = 5.66$, but could not proceed any further. A comparison of the absolute positions and shapes of the smaller drop in the (x, z)-plane for the two simulations is shown in the top row of figure 19 at different times. The convergence is excellent for $t = 3$ and 4, but has deteriorated somewhat at $t = 5$ and 5.5. The bottom row of figure 19 shows results using the traditional integral form (2.5), with the curvature calculated by the best paraboloid fitting but leaving the mesh stabilization method (5.3) and the rest of the code unchanged. Comparison of the top (a) and bottom (b) frames at $t = 3$ and 4 in figure 19 shows a much better convergence for the curvatureless method in these simulations, both in the absolute positions and the drop shapes. The contour at $t = 4$ using the traditional method and $N_{\Delta_1} = 2160$ is already corrupted, and this simulation could not be continued beyond $t = 4.06$, because of the errors in the curvature calculation and, as a consequence, a divergence of the velocity iterations. The simulation with $N_{\Delta_1} = 3840$ using the traditional
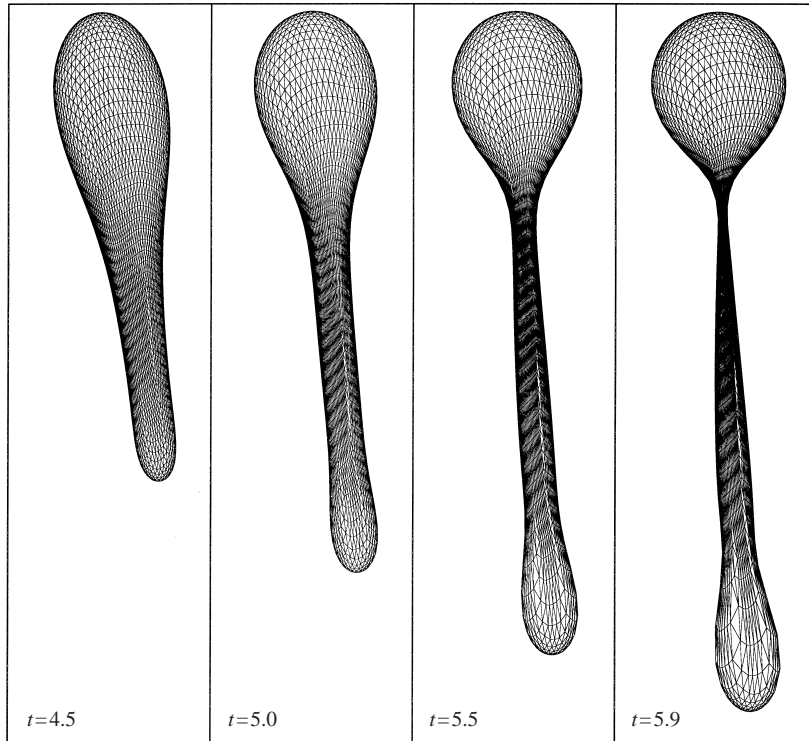
FIGURE 20. The same simulation as in figure 18, but with 6000 triangular elements on the smaller drop.

boundary-integral form (2.5) gives a smooth contour at $t = 4$ but still failed at $t \approx 4.1$ for the same reason.

The simulation of figure 19 further demonstrates that the traditional boundary-integral form with the curvature (2.5) cannot succeed in breakup simulations, if the mesh triangles are allowed to stretch; to be successful, this form would necessarily require dynamical mesh restructuring into compact elements (e.g. Cristini *et al.* 1998). In contrast, the present algorithm can proceed as close to breakup as needed, using a stretched mesh with fixed connections, provided that the fixed total number of elements is sufficiently large. In this example, we found it difficult to reach very thin necks with the limited triangulations $N_{\Delta_1} = 2160$ and 3840 (probably because the conditions are essentially supercritical, and the drop is quite long at breakup), but a more expensive run $N_{\Delta_1} = 6000$, $N_{\Delta_2} = 1280$ does proceed farther (figure 20); the drop shapes in the runs with $N_{\Delta_1} = 3840$ and 6000 practically coincide up to $t = 5.5$. Fortunately, very fine triangulations are not required to estimate the volume partition after the primary breakup in this simulation. As the neck radius becomes small, the dimensionless equivalent radius of the upper lobe (above the neck cross-section) extrapolates to $a_3/a_1 = 0.882$ ($N_{\Delta_1} = 2160$), 0.893 ($N_{\Delta_1} = 3840$) and 0.900 ($N_{\Delta_1} = 6000$), with good convergence at $N_{\Delta_1} \to \infty$; thus, the main fragment contains about 73% of the volume of the original drop.

Although the volume partition in the primary breakup can be reliably determined by the present code, we did not study this problem for two drops falling under gravity in detail, since the results may essentially depend on four parameters (a_1/a_2, λ, $\mathscr{B}$, and $\Delta\tilde{x}_o$). Instead, we examine here the critical conditions leading to breakup of
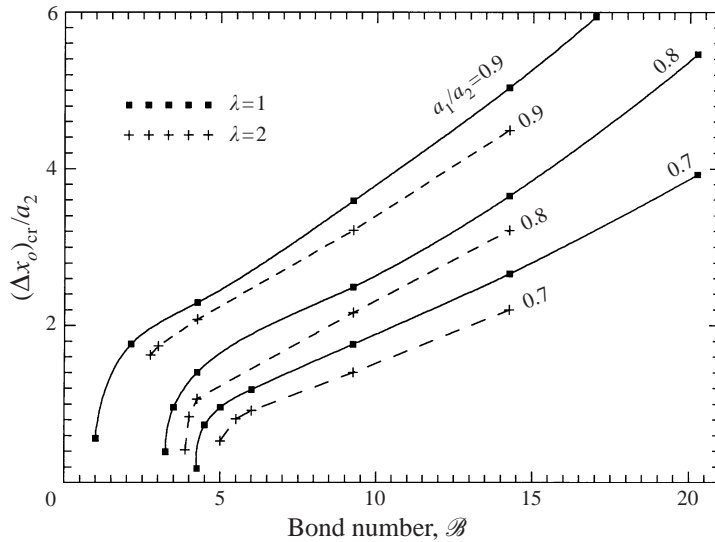
FIGURE 21. The non-dimensional critical offset, $\Delta x_o/a_2$, far upstream for the breakup of the smaller drop, as a function of the Bond number for different size ratios and viscosity ratios of $\lambda = 1$ and 2.

the smaller drop. Figure 21 presents the non-dimensional critical offset $(\Delta \tilde{x}_o)_{cr}$ far upstream as a function of the Bond number for different size ratios and two viscosity ratios $\lambda = 1$ and $\lambda = 2$. The initial vertical displacement was $\Delta \tilde{z}_o = 10$–15, and extrapolation to infinite initial separation was made by adding a relative trajectory for non-deformed drops. The margins demarcating the offsets with and without breakup were determined to ± 1–3% for $(\Delta \tilde{x}_o)_{cr} \geqslant 2$ and to a few percent for smaller $(\Delta \tilde{x}_o)_{cr}$; the latter case was the most difficult because the drops stay in very close contact for a long time on a critical trajectory. Most of the calculations were done with 1280 triangular elements on each drop. For large $\mathscr{B}$ and $a_1/a_2 = 0.8$–0.9, we used up to 2160 elements on each drop; less accurate calculations with $N_{\Delta_1} = N_{\Delta_2} = 1280$ could give an error of up to 5% in this case. For small $\mathscr{B}$ and $\lambda = 1$, we used 1280 elements on the larger and up to 3840 elements on the smaller drop. With extrapolation (see above), the effect of the finite initial displacement $\Delta \tilde{z}_o = 10$–15 was found to be negligible. The results indicate that the critical offset for breakup is a strong function of the Bond number and size ratio; as either the Bond number or size ratio is decreased, the resistance of the smaller drop to stretching is increased and the breakup efficiency decreases. Besides, the more detailed calculations for $\lambda = 1$ demonstrate the existence of critical values $\mathscr{B}_{br}(a_1/a_2, \lambda)$ with $(\Delta \tilde{x}_o)_{cr} = 0$, where breakup due to hydrodynamical interactions in buoyancy-driven motion does not occur, if the Bond number is less than the critical value $\mathscr{B}_{br}(a_1/a_2, \lambda)$. For supercritical values of the Bond number, however, the high values of $(\Delta \tilde{x}_o)_{cr}$ suggest that drop breakup caused by hydrodynamical interactions may be an essential feature in dilute emulsions with narrow size distributions and will tend to increase the polydispersity.

Our experience also suggests that artificial volume rescaling should be avoided in critical breakup calculations, at least in the present case of two drops settling under gravity. This rescaling is possibly justified in generic long-time boundary-integral calculations for compact shapes, but it artificially propagates the local errors in the shape calculation onto the entire surface, which is physically dubious for
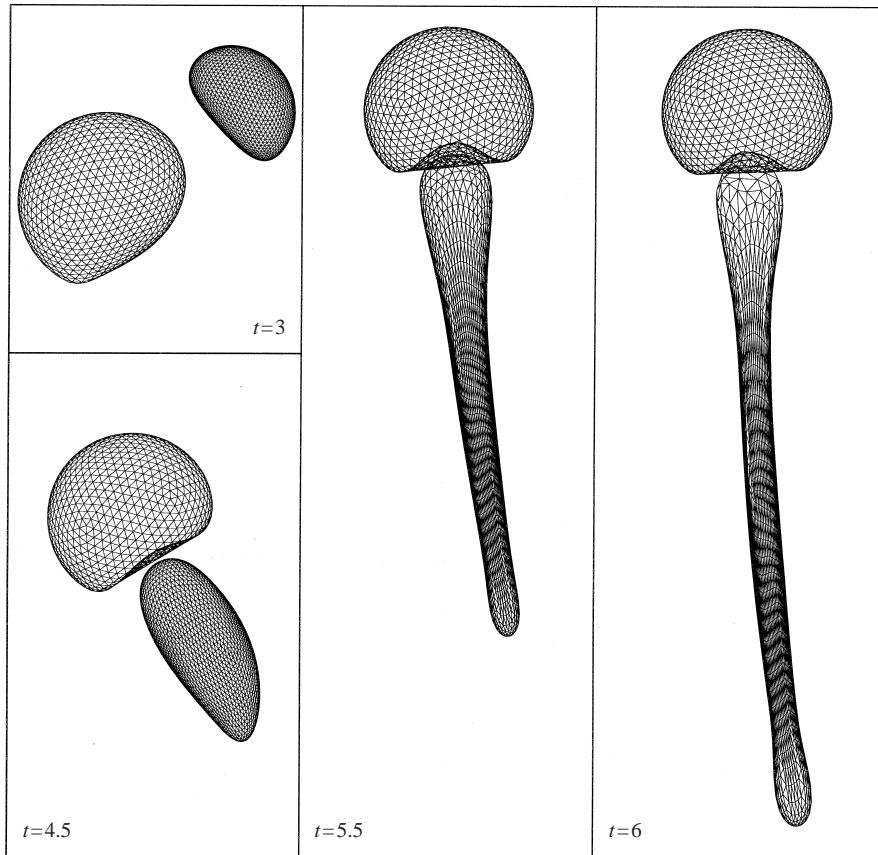
FIGURE 22. The combined capture and breakup phenomenon for two drops in buoyancy-driven motion with $a_1/a_2 = 0.7$, $\mathscr{B} = 7$, $\lambda = 0.3$, $\Delta\tilde{x}_o = 1.6$, and $\Delta\tilde{z}_o = 10$ by the curvatureless algorithm with 2160 triangular elements on the larger drop and 3840 elements on the smaller drop.

elongated drops. More seriously, this rescaling can lead to quantitatively wrong results for feasible triangulations. For example, when $\mathscr{B} = 5$, $a_1/a_2 = 0.7$, $\lambda = 2$, and $\Delta\tilde{z}_o = 10$, we had the bounds (prior to extrapolation to the infinite initial separation) of $(\Delta\tilde{x}_o)_{\mathrm{cr}} = 0.59 \pm 0.03$ for triangulations of (i) $N_{\Delta_1} = 1280$, $N_{\Delta_2} = 720$, (ii) $N_{\Delta_1} = N_{\Delta_2} = 1280$, and (iii) $N_{\Delta_1} = 3840$, $N_{\Delta_2} = 1280$, without rescaling. With rescaling, we obtained quite differently $(\Delta\tilde{x}_o)_{\mathrm{cr}} < 0.47$ for $N_{\Delta_1} = N_{\Delta_2} = 1280$. Probably, since the breakup in this case occurs in the far field, where the ambient flow for the breaking drop is weak, this rescaling competes with the ambient flow and dramatically slows down the convergence to the correct solution. We did not use volume rescaling in the critical offset calculations, or in the examples discussed above.

6.3. *Combined capture and breakup*

In §6.1 and §6.2, the capture and breakup phenomena for two drops settling under gravity were considered separately. The simulation in figure 22 for $a_1/a_2 = 0.7$, $\mathscr{B} = 7$, $\lambda = 0.3$, $\Delta\tilde{x}_o = 1.6$, $\Delta\tilde{z}_o = 10$, $N_{\Delta_1} = 3840$, and $N_{\Delta_2} = 2160$ gives an interesting example of combined capture and breakup. Namely, after the smaller drop is swept around the larger one, it becomes sucked into the dimple formed on the larger drop, like in the pure capture phenomenon (§6.1), but simultaneously undergoes considerable

elongation and starts necking. This behaviour strongly suggests that the smaller drop will break without being released from the dimple, as has also been observed in axisymmetric simulations by Davis (1999). Since there is no relaxation, however, the drop is expected to be extremely long at breakup, and we stopped the calculations at $t = 5.96$, after about 12 h of CPU time on an Alpha DEC 5/333 workstation.

The phenomena of capture, breakup, and combined capture and breakup allow us to classify the behaviour of two interacting, initially well-separated drops under gravity as follows. For every size ratio a_1/a_2 and viscosity ratio λ, there are two critical Bond numbers, $\mathscr{B}_{\mathrm{br}}(a_1/a_2, \lambda)$ for breakup and $\mathscr{B}_{\mathrm{c}}(a_1/a_2, \lambda)$ for capture. If $\mathscr{B} < \mathscr{B}_{\mathrm{br}}$, no breakup of the smaller drop will occur no matter how small the initial offset is; if $\mathscr{B} < \mathscr{B}_{\mathrm{c}}$, there is no capture for any offset. To classify the relative trajectories, it is necessary to know the relation between $\mathscr{B}_{\mathrm{br}}$ and $\mathscr{B}_{\mathrm{c}}$. Extrapolation of the curves in figure 21 for $\lambda = 1$ to zero critical offsets $(\Delta \tilde{x}_o)_{\mathrm{cr}}$ gives an example of estimating $\mathscr{B}_{\mathrm{br}}$, but such calculations are quite difficult, especially for $\lambda \neq 1$ and $a_1/a_2 \approx 1$. Instead, it was suggested (Zinchenko *et al.* 1997) that the smaller drop initially be placed behind the larger one in close contact, and then determining $\mathscr{B}_{\mathrm{br}}$ as the value demarcating the trajectories of the smaller drop with and without breakup. This concept turns out to be approximate, but gives a good and very efficient estimation of $\mathscr{B}_{\mathrm{br}}$ through the solution of the axisymmetrical problem, rather than by costly three-dimensional calculations; a similar method gives $\mathscr{B}_{\mathrm{c}}$. These axisymmetrical calculations (Davis 1999) show that $\mathscr{B}_{\mathrm{br}}$ is always appreciably smaller than $\mathscr{B}_{\mathrm{c}}$ for $\lambda = O(1)$ and size ratios not very close to unity. Thus, assuming $\mathscr{B}_{\mathrm{br}} < \mathscr{B}_{\mathrm{c}}$, the different modes of three-dimensional relative motion of two drops with $\lambda = O(1)$ can be classified as follows:

(1) $\mathscr{B} < \mathscr{B}_{\mathrm{br}}$. The drops separate, and there is no breakup and no capture for any initial offsets.

(2) $\mathscr{B}_{\mathrm{br}} < \mathscr{B} < \mathscr{B}_{\mathrm{c}}$. There is a critical initial breakup offset $(\Delta \tilde{x}_o)^{\mathrm{br}}_{\mathrm{cr}}$, but no capture for any offsets.

(3) $\mathscr{B} > \mathscr{B}_{\mathrm{c}}$. There is a critical offset, $(\Delta \tilde{x}_o)^{\mathrm{c}}_{\mathrm{cr}}$, for capture and a larger one, $(\Delta \tilde{x}_o)^{\mathrm{br}}_{\mathrm{cr}}$, for breakup. The trajectories with $\Delta \tilde{x}_o > (\Delta \tilde{x}_o)^{\mathrm{br}}_{\mathrm{cr}}$ will separate without capture and breakup. For $(\Delta \tilde{x}_o)^{\mathrm{c}}_{\mathrm{cr}} < \Delta \tilde{x}_o < (\Delta \tilde{x}_o)^{\mathrm{br}}_{\mathrm{cr}}$, drop breakup and separation will occur. The case $\Delta \tilde{x}_o < (\Delta \tilde{x}_o)^{\mathrm{c}}_{\mathrm{cr}}$ will give a combined capture and breakup phenomenon similar to that in figure 22.

The relation $\mathscr{B}_{\mathrm{br}} < \mathscr{B}_{\mathrm{c}}$ indicates that, for $\lambda = O(1)$, drop breakup caused by hydrodynamical interactions in buoyancy-driven motion should be more frequently observed than the deformation-induced capture. On the other hand, $\mathscr{B}_{\mathrm{br}} \to \infty$ at $\lambda \to 0$, and breakup is insignificant for low-viscosity drops and bubbles. The case $\lambda \gg 1$ is less interesting, since viscous damping prevents such drops from experiencing significant deformations.

7. Conclusions

A three-dimensional boundary-integral algorithm for interacting deformable drops at small Reynolds number has been developed, based on a new curvatureless formulation of the boundary-integral equations. Unlike the traditional formulation, the new form requires only the normal vectors, which are generally much less sensitive than the curvature to discretization errors. A regularization has been found to overcome difficulties with the higher singularity of the new form and make it applicable to any viscosity ratio λ and arbitrary surface separations. For slightly deformable drops, capable of approaching very small separations, the traditional

boundary-integral formulation is advantageous, since it gives more accurate thin film dynamics between nearly touching drops, although the curvatureless algorithm is still robust in this case. In contrast, for large deformations, or cusped interfaces, we give preference to the curvatureless formulation. In fact, the use of the new formulation is crucial (and, at present, appears to be the only way to proceed), if line singularities (sharp edges) develop on the surfaces. These singularities typically occur for low drop-to-medium viscosity ratios at high and moderately high Bond numbers, as shown both by our calculations and experiments (Manga & Stone 1993, 1995b), and produce a numerically unresolvable contribution (capillary force), invalidating the use of the traditional boundary-integral formulation. The new formulation eliminates this difficulty and, when combined with a dynamical smoothing procedure, provides a successful method for boundary-integral problems with line singularities. Very good resolution and convergence of drop/bubble separation and shapes are achieved, except in the fine details of the cusp or tip regions. We did not explore if our approach is applicable to steady flows with cusps, or is only a method for unsteady flows to considerably delay the development of singularities, until predictions about the global behaviour can be made. Using the present code, the deformation-induced capture efficiency of bubbles and low-viscosity drops in buoyancy-driven motion has been calculated in a wide range of Bond numbers for the first time.

With the traditional boundary-integral formulation, difficulties also occur in three-dimensional breakup simulations, when mesh triangles are allowed to stretch with the drop; this makes the curvature calculation ill-conditioned and causes failure in the early stages of breakup. Dynamical mesh restructuring into compact elements is a possible remedy (Cristini *et al.* 1998). This method starts with a modest number of triangles, and then increases the number of elements as a drop stretches and regions of high curvature form. The present approach offers an alternative for highly stretched drops approaching breakup, using a mesh of triangles with a fixed number of elements and fixed connections. A special, adaptive passive mesh stabilization technique has been developed in the present work to control such a mesh of highly stretched triangles and keep them from degeneration. When combined with the curvatureless formulation and an improved best-paraboloid method for the normal vectors, this strategy allows the calculations to approach drop breakup as close as needed, provided that the number of boundary elements is sufficiently large. We have applied the present method to study the three-dimensional breakup of the smaller drop caused by hydrodynamical interaction with the larger one in buoyancy-driven motion, for $\lambda = O(1)$. The possibility of accurately determining both the breakup time and the volume partitioning in the primary breakup has been shown. The critical centre-to-centre offsets far upstream leading to breakup have been calculated for $\lambda = 1$ and 2. The calculations also suggest the existence of the combined capture and breakup, when the smaller drop breaks without being released from the dimple formed on the larger one. A general classification of possible modes of two-drop relative motion under gravity for $\lambda = O(1)$ is provided. We conclude from the calculations that drop breakup for $\lambda = O(1)$ should be more frequently observed than deformation-induced capture in dilute sedimenting systems.

It would be worthwhile in future work to determine which of two very distinct approaches, the present one based on passive mesh stabilization, or an alternative based on dynamic mesh restructuring (Cristini *et al.* 1998), would be more optimal for different situations. Using a mesh with fixed topology (no restructuring)

is advantageous in generic applications, when the drops may have large deformations but are still away from the final stages of breakup, since this approach avoids mesh refinement along the drop length (i.e. the direction of slow spatial variation of unknowns) and it is also logically simple. Our recent calculations (Zinchenko & Davis 1999) for up to 125 highly deformable drops, with typically 1000–2000 triangular elements per drop, sedimenting in a periodic box by a hybrid of economical multipole (Zinchenko 1994, 1998) and boundary-integral techniques demonstrate the efficiency of passive mesh stabilization incorporated in the algorithm. On the other hand, in breakup simulations, our method has a reduced accuracy in resolving small bulbous ends and the neck region in the longitudinal direction at the very final stages of pinchoff, and it would be difficult to proceed after the primary breakup, with the minimizing function in its present form (5.3); the use of mesh restructuring for these purposes may be indispensable. An ideal method for three-dimensional breakup would most likely combine the best features of the two approaches, with adding new nodes in the longitudinal direction, but at a slow rate as the drop stretches, thus leaving the elements essentially elongated; the use of the curvatureless formulation in these conditions would be crucial. Regardless of the method, detailed three-dimensional breakup simulations seem to require fine triangulations.

Finally, a few comments about applicability to physical systems are in order. For a suspending fluid such as water with low viscosity, the drops or bubbles must have radii less than about $100\,\mu m$ if the Reynolds number is to be small in normal gravity. Under these conditions, and with typical interfacial tensions, the Bond number is much less than unity. Thus, large deformations at small Reynolds numbers under normal gravity require much more viscous systems (such as oils and magma) and/or much smaller interfacial tensions (such as for nearly miscible fluids).

Appendix A. Gradient iterations for the unit normal

The minimum of (4.5) on the unit sphere is sought iteratively by a gradient method:

$$\boldsymbol{n}^{\nu+1} = \frac{\boldsymbol{p}}{||\boldsymbol{p}||}, \quad \boldsymbol{p} = \boldsymbol{n}^{\nu} - \delta \nabla^{\parallel}\left[F(\boldsymbol{n}^{\nu}) + \gamma ||\boldsymbol{n}^{\nu} - \boldsymbol{n}^{*}||^{4}\right], \tag{A 1}$$

where $\boldsymbol{n}^{\nu}$ is the νth iteration, $\nabla^{\parallel}$ is the projection of the gradient on the plane normal to $\boldsymbol{n}^{\nu}$, and δ is a small parameter fixed at 0.05 (to provide a reasonably optimal convergence). To calculate $\nabla F(\boldsymbol{n})$, let (x', y', z') undergo a small rotation of angle $d\Omega$ about $\boldsymbol{x}_{i}$. The coefficients C, D, and E minimizing (4.4) also change, and we have

$$\mathrm{d}F = \sum_{j \in \mathscr{A}_{i}} \frac{2(C x_{ij}'^{2} + D x_{ij}' y_{ij}' + E y_{ij}'^{2} - z_{ij}')}{||\boldsymbol{x}_{ij}||^{2}}$$

$$\times \left[\mathrm{d}C x_{ij}'^{2} + \mathrm{d}D x_{ij}' y_{ij}' + \mathrm{d}E y_{ij}'^{2} + C\mathrm{d}(x_{ij}'^{2}) + D\mathrm{d}(x_{ij}' y_{ij}') + E\mathrm{d}(y_{ij}'^{2}) - \mathrm{d}z_{ij}\right]. \tag{A 2}$$

Partial derivatives of the right-hand side of function (4.4) with respect to C, D, and E are zero, and so the increments $\mathrm{d}C$, $\mathrm{d}D$, and $\mathrm{d}E$ do not contribute to (A 2).

Substituting kinematic relations

$$dx'_{ij} = -z'_{ij}d\Omega'_y + y'_{ij}d\Omega'_z, \quad dy'_{ij} = z'_{ij}d\Omega'_x - x'_{ij}d\Omega'_z, \quad dz'_{ij} = -y'_{ij}d\Omega'_x + x'_{ij}d\Omega'_y \quad (A\,3)$$

(where $d\Omega'_x$, $d\Omega'_y$, $d\Omega'_z$ are the (x', y', z') components of $d\Omega$) in (A 2) yields

$$dF = \sum_{j \in \mathscr{A}_i} \frac{2(Cx'^2_{ij} + Dx'_{ij}y'_{ij} + Ey'^2_{ij} - z_{ij})}{||\boldsymbol{x}_{ij}||^2}$$

$$\times \left[d\Omega'_x(Dx'_{ij}z'_{ij} + 2Ey'_{ij}z'_{ij} + y'_{ij}) - d\Omega'_y(2Cx'_{ij}z'_{ij} + Dy'_{ij}z'_{ij} + x'_{ij}) \right]. \quad (A\,4)$$

In deriving (A 4), we again made use of the fact that C, D, and E minimize (4.4); as expected, (A 4) does not contain $d\Omega'_z$. Since $d\boldsymbol{n} = (d\Omega'_y, -d\Omega'_x, 0)$, the expression (A 4) immediately gives $\nabla F(\boldsymbol{n})$ in the intrinsic coordinates (x', y', z'), which can be converted to the original coordinate system to perform the iterations in (A 1). The number of iterations in (A 1) is typically much larger than with the best-paraboloid method (Zinchenko *et al.* 1997), but this $O(MN)$ part of the calculation is still fast, compared to the $O(M^2N^2)$ boundary integral part, if the initial approximations to $\boldsymbol{n}$ are taken from the preceding time step.

Appendix B. Minimization of the mesh stabilization function

To minimize (5.3), F should be known as a function of the velocities $\boldsymbol{V}_i = d\boldsymbol{x}_i/dt$. More specifically, each part of (5.3) can be written as a quadratic function of $\boldsymbol{V}_1, \boldsymbol{V}_2, \dots \boldsymbol{V}_M$. This is obvious for (5.3b) (cf. with (5.1)). For (5.3c), we note that the quality function Q_Δ for a triangle with vertices $\boldsymbol{x}_{i_0}$, $\boldsymbol{x}_{i_1}$, and $\boldsymbol{x}_{i_2}$ is a simple known function of $\boldsymbol{R}_1 = \boldsymbol{x}_{i_1} - \boldsymbol{x}_{i_0}$ and $\boldsymbol{R}_2 = \boldsymbol{x}_{i_2} - \boldsymbol{x}_{i_0}$, and so

$$\frac{dQ_\Delta}{dt} = \frac{\partial Q_\Delta}{\partial \boldsymbol{R}_1} \cdot \left(\boldsymbol{V}_{i_1} - \boldsymbol{V}_{i_0} \right) + \frac{\partial Q_\Delta}{\partial \boldsymbol{R}_2} \cdot \left(\boldsymbol{V}_{i_2} - \boldsymbol{V}_{i_0} \right). \quad (B\,1)$$

Substituting (B 1) into (5.3c) gives a quadratic function of $\boldsymbol{V}_1, \dots \boldsymbol{V}_M$. If the neighbours of $\boldsymbol{x}_i$ are $\boldsymbol{x}_{j_1}, \dots \boldsymbol{x}_{j_L}$ (where L is the coordination number, 5 or 6 for our meshes), then the best-plane normal $\boldsymbol{n}_i^*$ at node $\boldsymbol{x}_i$ is only a function of $\boldsymbol{x}_{ij_k} = \boldsymbol{x}_{j_k} - \boldsymbol{x}_i$ $(k = 1, \dots L)$, and so

$$\frac{d\boldsymbol{n}_i^*}{dt} = \frac{\partial \boldsymbol{n}_i^*}{\partial \boldsymbol{x}_{ij_k}} \cdot \left(\boldsymbol{V}_{j_k} - \boldsymbol{V}_i \right). \quad (B\,2)$$

Using a similar expression for $d\boldsymbol{n}_j^*/dt$ and performing other time differentiations in (5.3a), this part can also be expressed as a quadratic function of $\boldsymbol{V}_1, \dots \boldsymbol{V}_M$. To calculate the derivatives $\partial \boldsymbol{n}_i^*/\partial \boldsymbol{x}_{ij_k}$, let (x'', y'', z'') be an intrinsic coordinate system with the origin at $\boldsymbol{x}_i$ and the z''-axis along $\boldsymbol{n}_i^*$ (unlike the (x', y', z')-system considered in §4). Projecting (4.3) on the (x'', y'')-plane and using (4.2) gives the equations

$$\sum_{j \in \mathscr{A}_i} \frac{x''_{ij}z''_{ij}}{||\boldsymbol{x}_{ij}||^2} = 0, \quad \sum_{j \in \mathscr{A}_i} \frac{y''_{ij}z''_{ij}}{||\boldsymbol{x}_{ij}||^2} = 0, \quad (B\,3)$$

where $\boldsymbol{x}_{ij} = (x''_{ij}, y''_{ij}, z''_{ij})$. A small change $\delta\boldsymbol{x}_{ij_0} = (\delta x''_{ij_0}, \delta y''_{ij_0}, \delta z''_{ij_0})$ in the position of one neighbour $j_0 \in \mathscr{A}_i$ causes a rotation of the intrinsic coordinate system (x'', y'', z'') of angle $d\Omega'' = (d\Omega''_x, d\Omega''_y, d\Omega''_z)$. This rotation changes the intrinsic coordinates of all neighbours $j \in \mathscr{A}_i$ by dx''_{ij}, dy''_{ij}, dz''_{ij}. For $j = j_0$, however, there is an additional,

direct contribution due to the change δx_{ij_0} of x_{ij_0}, and so

$$\left.\begin{array}{l} \mathrm{d}x''_{ij} = y''_{ij}\mathrm{d}\Omega''_z - z''_{ij}\mathrm{d}\Omega_y + \delta_{jj_0}\delta x''_{ij_0}, \\[2mm] \mathrm{d}y''_{ij} = z''_{ij}\mathrm{d}\Omega''_x - x''_{ij}\mathrm{d}\Omega''_z + \delta_{jj_0}\delta y''_{ij_0}, \\[2mm] \mathrm{d}z''_{ij} = x''_{ij}\mathrm{d}\Omega''_y - y''_{ij}\mathrm{d}\Omega''_x + \delta_{jj_0}\delta z''_{ij_0}. \end{array}\right\} \tag{B4}$$

Upon substitution of $x''_{ij} + \mathrm{d}x''_{ij}$, $y''_{ij} + \mathrm{d}y''_{ij}$, $z''_{ij} + \mathrm{d}z''_{ij}$ into (B3) and linearizing, the terms with $\mathrm{d}\Omega''_z$ do not contribute, and the resulting system of two linear equations can be solved for $\mathrm{d}\Omega''_x$ and $\mathrm{d}\Omega''_y$ in terms of $\delta x''_{ij_0}, \delta y''_{ij_0}, \delta z''_{ij_0}$. Since $\mathrm{d}n_i^* = (\mathrm{d}\Omega''_y, -\mathrm{d}\Omega''_x, 0)$, the relation between $\mathrm{d}n_i^*$ and $(\delta x''_{ij_0}, \delta y''_{ij_0}, \delta z''_{ij_0})$ can be used to calculate $\partial n_i^* / \partial x_{ij_0}$ in the fixed coordinate system which coincided with (x'', y'', z'') prior to the change of x_{ij_0}. The tensor $\partial n_i^* / \partial x_{ij_0}$ can be then converted to the original coordinates.

Once F is known as a quadratic function of $V_1, \ldots V_M$, the minimum of (5.3) under the constraints (5.2) can be found by conjugate gradient iterations, as described by (36)–(37) and (39) of Zinchenko *et al.* (1997). Note that the present method operates with two normals, the best-plane normal n^* in (5.3) and the more accurate normal n (§4) in (5.2) and the rest of the boundary-integral code. Using n in (5.3) would make the method more difficult, since n_i is a much more complex function of x_{ij_k}. The number of conjugate gradient iterations may be large for high aspect ratios, but the $O(MN)$ cost of mesh stabilizations is typically still small compared with the boundary-integral part (§2), even for $\lambda = 1$.

Appendix C. Time-step strategy

In non-dimensional variables (§6), with the larger non-deformed radius a_2 as the lengthscale, the time step primarily used in our calculations was

$$\Delta t = c_{\Delta t}(1 + \lambda)\mathscr{B}\min(\Delta x_1, \Delta x_2)/(8\pi), \tag{C1}$$

where $c_{\Delta t} = O(1)$ is a numerical factor (ranging typically from 1.5 (for $\lambda \ll 1$) to 2 (for $\lambda > 1$);

$$\Delta x_1 = \min_i \frac{h_i}{k_i a(i)}, \tag{C2}$$

the minimum is taken over all mesh vertices i on both drops, h_i is the minimum height of mesh triangles drawn from node i, k_i is the maximum curvature estimation (5.5) at node i, $a(i)$ is a_1/a_2 on drop 1 and unity on drop 2;

$$\Delta x_2 = V_{12}^\infty \frac{a_1}{a_2} \min_{i,j} \frac{h_i r_{ij}^2}{a(i)|r_{ij}\cdot(V_j - V_i)|}, \tag{C3}$$

where

$$V_{12}^\infty = \frac{16\pi[1 - (a_1/a_2)^2](\lambda + 1)}{9\left(\lambda + \frac{2}{3}\right)} \tag{C4}$$

is the non-dimensional relative velocity of isolated drops, and the minimum in (C3) is over all pairs (i, j) of mesh vertices on different surfaces separated by the radius-vector r_{ij}. The form (C1) includes the standard requirement $\Delta t \leqslant K\Delta x$, but K is a complicated function of the drop shapes and meshes. In particular, when the singularity forms, the time step should be greatly reduced, which is provided by (C2).

The form (C 3) serves to limit the time step for very small gaps δ. Since

$$\frac{\boldsymbol{r}_{ij}^2}{\boldsymbol{r}_{ij} \cdot (\boldsymbol{V}_j - \boldsymbol{V}_i)} = \frac{r_{ij}}{\mathrm{d}r_{ij}/\mathrm{d}t}, \qquad (C 5)$$

the near-contact motion of two slightly deformable drops with $\lambda = O(1)$ requires $\Delta t \sim \delta^{1/2}$, as in Zinchenko *et al.* (1997). For larger deformations and $\lambda = O(1)$, however, flattening occurs in the gap region, with small $\mathrm{d}\delta/\mathrm{d}t$, and so Δx_2 does not impose a limitation on the time step.

We have found the criterion (C 1) to give a stable and fairly optimal time step for most of the applications considered in §6. For drops closely approaching breakup, using (C 1) may appear to lead to instability. This instability, however, is due to insufficient triangulations in the neck region (as discussed in §6.2) and is eliminated when more elements are used.

REFERENCES

ACRIVOS, A. & LO, T. S. 1978 Deformation and breakup of a single drop in an extensional flow. *J. Fluid Mech.* **86**, 641–642.

ASCOLI, E. P., DANDY, D. S. & LEAL, L. G. 1990 Buoyancy-driven motion of a deformable drop toward a planar wall at low Reynolds number. *J. Fluid Mech.* **213**, 287.

BRENNER, M. P., LISTER, J. R. & STONE, H. A. 1996 Pinching threads, singularities and the number 0.0304... *Phys. Fluids* **8**, 2827–2836.

BRUIJN DE, R. A. 1993 Tipstreaming of drops in simple shear flows. *Chem. Engng Sci.* **48**, 277–284.

BUCKMASTER, J. D. 1972 Pointed bubbles in slow viscous flow. *J. Fluid Mech.* **55**, 385–400.

BUCKMASTER, J. D. 1973 The bursting of pointed drops in slow viscous flow. *Trans. ASME* E: *J. Appl. Mech.* **40**, 18–24.

CHI, B. K. & LEAL, L. G. 1989 A theoretical study of the motion of a viscous drop toward a fluid interface at low Reynolds number. *J. Fluid Mech.* **201**, 123–146.

COULLIETTE, C. & POZRIKIDIS, C. 1998 Motion of an array of drops through a cylindrical tube. *J. Fluid Mech.* **358**, 1–28.

CRISTINI, V., BLAWZDZIEWICZ, J. & LOEWENBERG, M. 1998 Drop breakup in three-dimensional viscous flows. *Phys. Fluids* **10**, 1781–1783.

DAVIS, R. H. 1999 Buoyancy-driven viscous interaction of a rising drop with a smaller trailing drop. *Phys. Fluids* **11**, 1016–1028.

EGGERS, J. 1993 Universal pinching of three-dimensional axisymmetric free-surface flow. *Phys. Rev. Lett.* **71**, 3458–3460.

EGGERS, J. 1997 Non-linear dynamics and breakup of free-surface flows. *Rev. Mod. Phys.* **69**, 865–929.

HINCH, E. J. & ACRIVOS, A. 1979 Steady long slender droplets in two-dimensional straining motion. *J. Fluid Mech.* **91**, 401–414.

JEONG, J.-T. & MOFFATT, H. K. 1992 Free-surface cusps associated with flow at low Reynolds number. *J. Fluid Mech.* **241**, 1–22.

JOSEPH, D. D., NELSON, J., RENARDY, M. & RENARDY, Y. 1991 Two-dimensional cusped interfaces. *J. Fluid Mech.* **223**, 383–409.

JOSEPH, D. D. & RENARDY, Y. Y. 1993 *Fundamentals of Two-Fluid Dynamics*. Springer.

KELMANSON, M. A. 1983*a* Modified integral equation solution of viscous flows near sharp corners. *Comput. Fluids* **11**, 307–324.

KELMANSON, M. A. 1983*b* An integral equation method for the solution of singular slow flow problems. *J. Comput. Phys.* **51**, 139–158.

KENNEDY, M. R., POZRIKIDIS, C. & SKALAK, R. 1994 Motion and deformation of liquid drops, and the rheology of dilute emulsions in simple shear flow. *Comput. Fluids* **23**, 251–278.

KOCH, D. M. & KOCH, D. L. 1995 Numerical and theoretical solutions for a drop spreading below a free fluid surface. *J. Fluid Mech.* **287**, 251–278.

Koh, C. J. & Leal, L. G. 1989 The stability of drop shapes for translation at zero Reynolds number through a quiescent fluid. *Phys. Fluids* A **1**, 1309–1313.

Li, X. & Pozrikidis, C. 1997 The effect of surfactants on drop deformation and on the rheology of dilute emulsions in Stokes flow. *J. Fluid Mech.* **341**, 165–194.

Lister, J. R. & Stone, H. A. 1998 Capillary breakup of a viscous thread surrounded by another viscous fluid. *Phys. Fluids* **10**, 2758–2764.

Loewenberg, M. & Hinch, E. J. 1996 Numerical simulation of a concentrated emulsion in shear flow. *J. Fluid Mech.* **321**, 395–419.

Loewenberg, M. & Hinch, E. J. 1997 Collision of two deformable drops in shear flow. *J. Fluid Mech.* **338**, 299–315.

Manga, M. 1997 Interactions between mantle diapirs. *Geophys. Res. Lett.* **24**, 1871–1874.

Manga, M. & Stone, H. A. 1993 Buoyancy-driven interactions between two deformable viscous drops. *J. Fluid Mech.* **256**, 647–683.

Manga, M. & Stone, H. A. 1995a Low Reynolds number motion of bubbles, drops and rigid spheres through fluid-fluid interfaces. *J. Fluid Mech.* **287**, 279–298.

Manga, M. & Stone, H. A. 1995b Collective hydrodynamics of deformable drops and bubbles in dilute low Reynolds number suspensions. *J. Fluid Mech.* **300**, 231–263.

Milliken, W. J., Stone, H. A. & Leal, L. G. 1993 The effect of surfactant on the transient motion of Newtonian drops. *Phys. Fluids* A **5**, 69–79.

Noh, D. S., Kang, I. S. & Leal, L. G. 1993 Numerical solutions for the deformation of a bubble rising in dilute polymeric fluids. *Phys. Fluids* A **5**, 1315–1332.

Papageorgiou, D. T. 1995 On the breakup of viscous liquid threads. *Phys. Fluids* **7**, 1529–1544.

Pawar, Y. & Stebe, K. J. 1996 Marangoni effects on drop deformation in an extensional flow: The role of surfactant physical chemistry. I. Insoluble surfactants. *Phys. Fluids* **8**, 1738.

Pozrikidis, C. 1990a The deformation of a liquid drop moving normal to a plane wall. *J. Fluid Mech.* **215**, 331.

Pozrikidis, C. 1990b The instability of a moving viscous drop. *J. Fluid Mech.* **210**, 1–21.

Pozrikidis, C. 1992 *Boundary Integral and Singularity Methods for Linearized Viscous Flow.* Cambridge University Press.

Pozrikidis, C. 1993 On the transient motion of ordered suspensions of liquid drops. *J. Fluid Mech.* **246**, 301–320.

Pozrikidis, C. 1997 Numerical studies of singularity formation at free surfaces and fluid interfaces in two-dimensional Stokes flow. *J. Fluid Mech.* **331**, 145–167.

Pozrikidis, C. 1998 Numerical studies of cusp formation at fluid interfaces in Stokes flow. *J. Fluid Mech.* **357**, 29–57.

Rallison, J. M. 1981 A numerical study of the deformation and burst of a viscous drop in general shear flows. *J. Fluid Mech.* **109**, 465–482.

Rallison, J. M. & Acrivos, A. 1978 A numerical study of the deformation and burst of a viscous drop in an extensional flow. *J. Fluid Mech.* **89**, 191–200.

Richardson, S. 1968 Two dimensional bubbles in slow flow. *J. Fluid Mech.* **33**, 475–493.

Richtmyer, R. D. & Morton, K. W. 1967 *Difference Methods for Initial Value Problems.* Interscience.

Rother, M. A., Zinchenko, A. Z. & Davis, R. H. 1997 Buoyancy-driven coalescence of slightly deformable drops. *J. Fluid Mech.* **346**, 117–148.

Sherwood, J. D. 1981 Spindle shaped drops in a viscous extensional flow. *Math. Proc. Camb. Phil. Soc.* **90**, 529–536.

Sherwood, J. D. 1984 Tip streaming from slender drops in a non-linear extensional flow. *J. Fluid Mech.* **144**, 281–295.

Stone, H. A. 1994 Dynamics of drop deformation and breakup in viscous fluids. *Ann. Rev. Fluid Mech.* **26**, 65–102.

Stone, H. A. & Leal, L. G. 1989a Relaxation and breakup of an initially extended drop in an otherwise quiescent fluid. *J. Fluid Mech.* **198**, 399–427.

Stone, H. A. & Leal, L. G. 1989b The influence of initial deformation on drop breakup in subcritical time-dependent flows at low Reynolds numbers. *J. Fluid Mech.* **206**, 223–263.

Stone, H. A. & Leal, L. G. 1990 The effects of surfactants on drop deformation and breakup. *J. Fluid Mech.* **220**, 161–186.

TJAHJADI, M., STONE, H. A. & OTTINO, J. M. 1992 Satellite and subsatellite formation in capillary breakup. *J. Fluid Mech.* **243**, 297–317.

UNVERDI, S. O. & TRYGGVASON, G. 1992 A front-tracking method for viscous, incompressible, multi-fluid flows. *J. Comput. Phys.* **100**, 25–37.

ZHANG, X. & DAVIS, R. H. 1991 The rate of collisions of small drops due to Brownian or gravitational motion. *J. Fluid Mech.* **230**, 479–504.

ZHOU, H. & DAVIS, R. H. 1996 Axisymmetric thermocapillary migration of two deformable viscous drops. *J. Colloid Interface Sci.* **181**, 60–72.

ZINCHENKO, A. Z. 1982 Calculations of the effectiveness of gravitational coagulation of drops with allowance for internal circulation. *Prikl. Mat. Mech.* **46**, 58–65.

ZINCHENKO, A. Z. 1994 An efficient algorithm for calculating multiparticle thermal interaction in a concentrated dispersion of spheres. *J. Comput. Phys.* **111**, 120–135.

ZINCHENKO, A. Z. 1998 Effective conductivity of loaded granular materials by numerical simulation. *Phil. Trans. R. Soc. Lond.* A **356**, 2953–2998.

ZINCHENKO, A. Z. & DAVIS, R. H. 1999 An efficient algorithm for hydrodynamical interaction of many deformable drops. *J. Comput. Phys.* (under review).

ZINCHENKO, A. Z., ROTHER, M. A. & DAVIS, R. H. 1997 A novel boundary-integral algorithm for viscous interaction of deformable drops. *Phys. Fluids* **9**, 1493–1511.